ANALYSIS OF FLOW IN OPEN-END PRESSURE SWIRL ATOMIZERS

MUSTAFA AYKAN UZUN

ÖZYEĞİN UNIVERSITY

FEBRUARY, 2025

ANALYSIS OF FLOW IN OPEN-END PRESSURE SWIRL ATOMIZERS

by
Mustafa Aykan Uzun

Thesis
Submitted in Partial Fulfillment of the
Requirements for the Degree of

Master of Science

in
Mechanical Engineering

Advisor: Assoc. Prof. Özgür Ertunç

Graduate School of Science and Engineering
Özyeğin University
İstanbul

February, 2025

ANALYSIS OF FLOW IN OPEN-END PRESSURE SWIRL ATOMIZERS

Approved by:

Assoc. Prof. Özgür Ertunç, Advisor
Department of Mechanical Eng.
Özyeğin University

Asst. Prof. Altuğ Melik Başol
Department of Mechanical Eng.
Özyeğin University

Prof. Oğuz Uzol
Department of Aerospace Eng.
Middle East Technical University

Approval Date: December 27, 2024

DECLARATION OF ORIGINALITY

I hereby declare that I am the sole author of this thesis and that this is the true copy of my thesis, including the final revisions, approved by my thesis committee. All data and information have been obtained, produced, and presented in accordance with the rules of research ethics and principles of academic honesty. As required by these rules, to the best of my knowledge I have acknowledged ideas, thoughts, and any copyrighted material in accordance with the standard referencing rules. I certify that any part of this thesis has not been submitted for a degree or diploma in another educational institution.

Mustafa Aykan Uzun

ABSTRACT

In this study, high-fidelity 3D and 2D axisymmetric open-end pressure swirl atomizer CFD simulations were performed. The low Reynolds number multiphase liquid flow is captured with the VOF method and second-order accurate direct solution of the incompressible Navier-Stokes equations (Quasi-DNS). The study aims to investigate the internal flow characteristics of PSA without inlet and contraction effects. Because in PSA, swirling liquid film flow is generated with a finite number of tangential inlet ports. These ports generate jet flows, which are one of the leading reasons for flow instabilities in liquid film. These instabilities are the results of spray non-uniformity in PSA. To remove these effects, continuous ring-like axisymmetric inlet surface and axial inlet surface with liquid film tangential, axial velocity, and volume fraction profile are used in 3D simulations. The volume fraction and velocity profiles are obtained from the swirling liquid film of ring-like inlet PSA simulations. In ring-like inlet simulations, Görtler vortices are captured within the liquid film and obtained that the instability source of these vortices is flow separation near the inlet. Development of Görtler vortices without referred instability source is examined in 3D axial inlet PSA simulations. Conclude that Görtler vortices initiate itself even without inlet separation. Görtler number is computed in the swirling liquid film to compare the results obtained with those in the literature. The Görtler number is modified which will be suitable for two-phase swirling film flow. After that, the effect of Görtler vortices on liquid film and spray is examined. The development of velocity profiles of liquid film through the exit of PSA is compared with 2D axisymmetric simulations, and Görtler vortices are observed to result in a linear velocity profile in film. However, it does not affect PSA's performance parameters. The pressure drop, film thickness, and spray angle of 2D axisymmetric simulations are predicted to be almost the same as those of 3D simulations. In the scope of these results, a new blade-type inlet for PSA is designed. By

utilizing the inlet type, uniform flow at the inlet is achieved. Due to the achievement, the PSA swirl atomizer can be accurately designed by utilizing 2D axisymmetric simulations, which are remarkably faster than 3D simulations. An experimental study was conducted to examine the performance of blade-type inlet PSA. The results of the experiments are compared with the 3D and 2D axisymmetric simulations.

Keywords: Görtler Vortices, Pressure, Swirl, Atomizer, Injector, CFD

ÖZET

Bu çalışmada, yüksek çözünürlüklü 3 boyutlu ve 2 boyutlu eksenel simetrik açık uçlu basınç girdaplı püskürtücülerin (PSA) hesaplamalı akışkanlar dinamiği simülasyonları gerçekleştirilmiştir. Düşük Reynolds sayısına sahip çok fazlı sıvı akışı, VOF yöntemi ve sıkıştırılamaz Navier-Stokes denklemlerinin ikinci mertebe doğru doğrudan çözümü (Quasi-DNS) kullanılarak modellenmiştir. Çalışma, basınç girdaplı püskürtücünün giriş ve daralma etkileri olmadan iç akış karakteristiklerini incelemeyi amaçlamaktadır. Çünkü basınç girdaplı püskürtücülerde dönen sıvı film akışı, sınırlı sayıda teğetsel giriş portu ile oluşturulmaktadır. Bu portlar, sıvı filmdeki akış kararsızlıklarının önde gelen nedenlerinden biridir. Bu kararsızlıklar, basınç girdaplı püskürtücülerde püskürtme düzensizliklerine neden olmaktadır. Bu etkileri ortadan kaldırmak için, 3 boyutlu simülasyonlarda sürekli halka benzeri eksenel simetrik giriş yüzeyi ve eksenel giriş yüzeyi kullanılmıştır. Eksenel giriş yüzeyi simulasyonlarında sıvı filmin teğetsel ve eksenel hız profilleri ile hacimsel oran profili kullanılmıştır. Hacimsel oran ve hız profilleri, halka benzeri giriş basınç girdaplı püskürtücü simülasyonlarının dönen sıvı filminden elde edilmiştir. Halka benzeri giriş simülasyonlarında, sıvı film içinde Görtler vorteksleri saptanmıştır. Bu vortekslerin kararsızlık kaynağının, giriş yakınındaki akış kopması olduğu tespit edilmiştir. Giriş kopması olmaksızın Görtler vortekslerinin gelişimi, 3 boyutlu eksenel giriş basınç girdaplı püskürtücü simülasyonlarında incelenmiştir. Görtler vortekslerinin, herhangi bir kararsızlık kaynağı olmaksızın kendiliğinden başladığı sonucuna varılmıştır. Dönen sıvı filmdeki Görtler sayısı hesaplanmış ve elde edilen sonuçlar literatür ile karşılaştırılmıştır. Görtler sayısı, iki fazlı dönen film akışına uygun olacak şekilde değiştirilmiştir. Daha sonra, Görtler vortekslerinin sıvı film ve püskürtme üzerindeki etkisi incelenmiştir. basınç girdaplı püskürtücü çıkışındaki sıvı filmin hız profillerinin gelişimi, 2 boyutlu eksenel simetrik simülasyonlarla karşılaştırılmıştır. Görtler vortekslerinin filmde doğrusal bir hız

profili oluşturduğu ancak basınç girdaplı püskürtücünün performans parametrelerini etkilemediği gözlemlenmiştir. 2 boyutlu eksenel simetrik simülasyonların basınç düşüşü, film kalınlığı ve püskürtme açısı sonuçlarının, 3 boyutlu simülasyonlarla neredeyse aynı olduğu öngörülmüştür. Bu sonuçlar kapsamında, basınç girdaplı püskürtücü için yeni bir kanat tipi giriş tasarlanmıştır. Bu giriş tipi kullanılarak girişte düzgün akış sağlanmıştır. Bu sayede basınç girdaplı püskürtücü, 3 boyutlu simülasyonlara kıyasla çok daha hızlı olan 2 boyutlu eksenel simetrik simülasyonlarla doğru bir şekilde tasarlanabilir. Kanat tipi giriş basınç girdaplı püskürtücünün performansını incelemek için deneysel bir çalışma gerçekleştirilmiştir. Deney sonuçları, 3 boyutlu ve 2 boyutlu eksenel simetrik simülasyonlarla karşılaştırılmıştır.

Anahtar Kelimeler: Görtler girdabı, Basınçlı, girdap, püskürtücü, Hesaplamalı Akışkanlar Dinamiği

ACKNOWLEDGEMENTS

I would like to express my deepest gratitude to my advisor, Assoc. Prof. Dr-Ing Özgür Ertunç, for his invaluable guidance, expertise, and encouragement throughout this research. His mentorship has been a cornerstone in the successful completion of this work.

I am profoundly grateful to my colleagues Aziz Mert Karul, Alper Akardere, Gökhan Kayansalçık, Deniz İmamoğlu, Velican Coşar, and Onur Şen, whose constructive discussions and insightful feedback have greatly enriched my research experience. Their collaboration and support have been vital to this study.

Special thanks to my teammate Kutay Anbarcı for his unwavering support during the experiments and his contributions to the manufacturing of test samples. His dedication and teamwork were instrumental in overcoming many challenges.

I would also like to acknowledge the Scientific and Technological Research Council of Turkey (TÜBİTAK-2224a) for their financial support, which enabled me to attend the 1st European Fluid Dynamics Conference. This opportunity was pivotal in advancing my academic and professional growth.

Finally, I wish to express my heartfelt thanks to my family for their unwavering support, encouragement, and understanding throughout this journey. Their belief in me has been my greatest source of strength.

TABLE OF CONTENTS

LIST OF TABLES

LIST OF FIGURES

LIST OF SYMBOLS

Latin Symbols:

c	: Pitch of helix
D	: Nozzle diameter
f_s	: Surface tension force
G	:Görtler number
H	: Helicity function
L	: Nozzle length
L_I	: Inlet length
L_d	: Length of domain
n^*	: Fluids interface normal vector
P	: Pressure
P_{flux}	: Momentum flow rate flux
R	: Nozzle radius
r	:Radial direction in cylindrical coordinate
R_c	: Radius of curvature
Re_{bulk}	: Bulk Reynolds number
R_d	: Radius of domain
Re_{film}	: Film thickness based Reynolds number
R_h	: Radius of helicity
S_u	: Mass source term
t_f	: Liquid film thickness
t_m	: Momentum thickness

U	: Velocity vector
V_{free}	: Free stream velocity
V_r	: Velocity vector in radial direction
V_z	: Velocity vector in axial direction
V_θ	: Velocity vector in tangential direction
w	: Weight function
z	:Axial direction in cylindrical coordinate

Greek Symbols:

α	: volume fraction of fluid phase
θ	:Angular direction in cylindrical coordinate
θ_f	: Inlet flow angle
θ_w	: Inlet side wall angle
κ_h	: Curvature of helix
κ_s	: Surface curvature
μ	: Dynamic viscosity of fluid
ν	: Kinematic viscosity of fluid
ρ	: Density of fluid
τ	: Shear stress vector
ω	: Vorticity vector

LIST OF ACRONYMS AND ABBREVIATIONS

CFD	Computational Fluid Dynamics
CLSVOF	Coupled Level Set and Volume of Fluid
CSF	Continuum Surface Force
DAQ	Data Acquisition
DNS	Direct Numeric Simulation
HRIC	High Resolution Interface Capturing
LES	Large Eddy Simulation
LISA	Linear Stability Analysis Sheet Atomization
LS	Level Set
IDDES	Improved Delayed Detached-Eddy Simulation
PSA	Pressure Swirl Atomizer
SMD	Sauter Mean Diameter
VOF	Volume of Fluid

1. INTRODUCTION

In the combustion of liquid fuel, bulk liquid is injected into the combustion chamber in such a way that it generates a form of droplets. The method, which is called liquid atomization, aims to increase the chemical reaction area between fuel and oxidizer. However, the size, velocity, and distribution of these droplets are critical to control the combustion process. In industry, various injector nozzles are used to perform liquid atomization. Pressure swirl atomizers are one of these nozzle types. It is widely used for fuel injection in combustion chambers where continuous combustion occurs, such as in liquid rocket engines and gas turbines.

1.1 Internal Flow Characteristics of Pressure Swirl Atomizers

The idea behind the design of pressure swirl atomizers (PSA) is to create cone-shaped spray films. In this way, the spray film becomes thinner as it goes far from the nozzle and breaks up to generate smaller droplets. However, to achieve this objective, the liquid film inside the PSA nozzle has to be stable and uniform to generate homogeneously distributed droplets. In the scenario of unstable liquid film spray, the film can break up before thinning enough, which causes relatively thick droplet formation. In non-uniform liquid film, inhomogeneous droplet distribution can be observed, and even more streaks can occur in the spray film. Therefore, the internal flow characteristics of PSA have to be well understood to create a proper spray film.

The PSA can be divided into two main types, which are open and closed type atomizers. The dominant flow regime inside PSA is swirling flow for both types. In a closed-type PSA, swirling flow is supplied by feeding pressurized liquid to the swirl chamber with tangential inlet ports. With the swirling flow, the liquid starts to rotate in a swirl chamber, and the tangential velocity of the flow increases toward its center. The

condition creates a low-pressure field at the center, lower than ambient pressure. Due to the pressure difference, gas fills towards the center, and it causes the liquid to stick to the wall with the help of centrifugal force caused by rotating motion. In this way, swirling liquid film flow occurs near the orifice wall. In the stability of the liquid film, centrifugal force has a vital role. Moreover, liquid film becomes thinner with increasing centrifugal force, which helps to produce smaller droplets. In this scope, Suyari and Lefebvre [1] have conducted an experimental study to measure film thickness and the effect on Sauter Mean Diameter (SMD) of droplet distribution. They control the centrifugal force on the film with port diameter. Because the swirl arm of the flow at the inlet increases with the smaller port diameter and results in a high angular momentum flow rate [2]. The results indicate that film thickness decreases with a smaller port diameter, and SMD decreases accordingly.

The closed-type PSA is advantageous in providing higher centrifugal force because tangential inlets are connected to the swirling chamber, which has a larger diameter than the orifice. In other words, liquid enters the PSA nozzle with a higher angular momentum flow rate, which means the liquid film is pushed to the orifice wall with higher centrifugal force. However, there is a contraction between the swirling chamber and the orifice; the flow accelerates to the orifice through a contraction. The condition results in a separation near the end of contraction if a proper contraction geometry is not designed. Yule et al. [3] have conducted a comparative numerical study on contraction geometry. He concluded that film instability increased in plain contraction compared to streamlined contraction, and conical geometry showed moderate performance, while there were no dramatic changes in major performance parameters, such as discharge coefficient. Qian et al. [4] investigated the cone angle in the contraction in their numerical study. He obtained that the recirculation vortex exists near the conical contraction, and the vortex causes waves on the liquid film. He determined that the size of the vortex decreases with

a smaller contraction angle so that the film becomes more stable.

In an open-type, PSA liquid is directly fed to the orifice via tangential ports. Thus, providing a higher angular momentum flow rate at the inlet is more difficult than closed-type PSA. To increase the angular momentum flow rate at the inlet port, the diameter has to be decreased significantly compared to the closed-type atomizer. The manufacture of these ports has become challenging with the decreasing diameter. Manufacturing tolerances of the port diameters remain the same in magnitude; however, the ratio of the manufacturing tolerance to the port diameter increases remarkably. The situation results in a high volatility in the performance parameter of PSA.

The manufacturing of open-type atomizers is more straightforward than that of closed-type PSA because open-type PSA can be machined as a single part. Moreover, open-type PSA can be easily manufactured in coaxial form to inject two liquid phases, which is required in liquid rocket engines. When open-type PSA nozzles are used, they can be manufactured as single parts, which is not possible in the manufacturing of close-type coaxial PSA. Therefore, leakage and assembly problems are mostly reduced in open-type coaxial PSA nozzles.

Inlet ports are discrete elements, and the liquid enters the orifice as a jet flow. Therefore, homogenization of momentum distribution in liquid film is a challenging factor in an open-type PSA. However, the swirl chamber of close type atomizer has a role not only in providing liquid entry with a higher angular momentum flow rate but also in behaving as a mixing chamber. On the other hand, liquid enters the orifice with tangential and radial velocity components at the inlet, and this radial velocity decelerates toward the center. Then, accelerates through the orifice wall due to the centrifugal force. Due to this behavior, separation of the flow is formed near the inlet. The separation is also one of the instability sources in the swirling liquid film flow. There is a lack of studies in open-type PSA; Fu et al. [5] have investigated the stability of liquid film in an open-type

PSA with an electrical conductance method. He examined the effect of pressure drop on the film stability. The results show that the film stabilizes in a pressure drop range. Accordingly, the stability of spray film has been examined by Fu et al. [6] experimentally. He represents the stability of the spray film as the ratio of angular momentum flow rate to axial momentum flow rate. Then, the stability of the spray film increases by raising the angular-to-axial momentum flow rate ratio. In this scope of results, open-type PSAs are not robust for varying mass flow rates. It should be designed with a proper tangential to axial momentum flow rate ratio at the desired flow rate.

1.2 Numerical Modelling of Pressure Swirl Atomizers

There is a two-phase immiscible swirling flow in PSA. The most critical part of numerical modeling of flow inside PSA and spray film is capturing the interface between the two phases. Three main models exist in the literature for capturing the interface. First, the Volume of Fluid (VOF) model is the most preferred one, presented by Hirt and Nichols [7]. In the VOF model, the interface is captured as a mesh cell and assumes that cell size sufficiently resolves the geometry of the interface. The interface is presented as a fraction occupied by phases. The physical properties of the interface, such as viscosity and density, are computed by volume averaging of the phases according to their volume fractions in the interface cell, and the Navier-Stokes equations are solved at the interface by using those averaged properties. The method has great performance in the conservation of mass and momentum of fluids. However, mesh resolution and time steps have to be relatively small. Otherwise, numerical diffusion of fluids occurs in the fluid domain, and the geometry of the interface cannot be captured accurately. The numerical diffusion can be artificially sharpened using the High-Resolution Interface Capturing (HRIC) scheme, which normalizes the face of an interface according to local Courant number [8]. The Level Set(LS) method is another option for modeling the interface. Sussman et al.

[9] have improved that method in which interface curvature can be captured accurately. Accurate curvature computation is essential in the numerical modeling of two-phase immiscible flows because surface tension is modeled as a function of curvature. However, the method is not eligible in mass conservation. Sussman et al. [10] have eliminated the mass conservation problem of the LS method by coupling the method with VOF. The method is the Coupled Level Set and Volume Fluid (CLSVOF) method. In that method, the level set function is discretized to compute the volume fraction of the interface.

The decision of which turbulence model to use in the numerical modeling of PSA and the specification of the fluid domain space are the remaining important criteria. 3D and 2D axisymmetric domains are used in literature. The cylindrical geometry of PSA enables the assumption of an axisymmetric flow in the solution of the Navier-Stokes equation. So that PSA simulations can be conducted in the 2D axisymmetric domain. In other words, gradients in angular direction are reduced in the Navier-Stokes equation, which provides a solution to the equation in 2D space. However, inlet ports disrupt the axial symmetry of the geometry. In the literature, the liquid is fed to the swirl chamber from its lateral surface. To provide identical conditions in that inlet with tangential port inlets, fluid properties and thickness of the inlet surface are determined using conservation laws of mass, angular momentum, and kinetic energy [11].

Observation of flow characteristics of PSA in terms of uniformity of the flow, droplet diameter distribution, or vortex structures in internal flow requires high-fidelity 3D simulations. On the other hand, 2D axisymmetric simulations are cheaper for computations of PSA performance parameters, which are discharge coefficient, film thickness, and spray angle. Even more, primary atomization and droplet distribution of the spray film can be predicted using primary atomization models such as LISA.

In the scope of referred advantages accuracy 2D axisymmetric simulations, it is widely investigated in the literature. Bal et al. [12] have examined the reliability of 2D

axisymmetric simulations on PSA performance parameters by comparing the results with 3D simulations and experiments. He used VOF model and Improved Delayed Detached-Eddy Simulation (IDDES). He concludes that there is a dramatic error in the results of 2D axisymmetric simulations. Because inlet properties of those simulations are determined according to conservation laws with uniform flow assumption at the 3D port inlets. However, he highlighted that flow separation exists in inlet ports, and there is no uniform velocity profile at the inlet. To eliminate the referred condition, he determined inlet properties according to conservation laws with exact velocity profiles of 3D inlet ports. When the 2D inlet properties are updated with exact 3D velocity profiles, he obtained that the results of 2D axisymmetric simulations and 3D simulations are relatively close to each other. When he compared simulation results with experiments. He obtained that discharge coefficient and spray angle are predicted with less than 5% error. And film thickness error is decreases with increasing Reynolds number up to less than 10%. Maly et al. [13] also pointed out the same issue. Determination of inlet properties of 2D axisymmetric simulations is crucial. He conducted 2D axisymmetric, 3D full sector, and 3D periodic simulations with various mesh configurations and turbulence models. He suggests that velocity profiles of 3D inlet ports are computed by conducting single-phase simulation for inlet geometry. Then, velocity profiles taken from this simulation are adapted to the 2D simulations. He reported that with that method,d closer results can be obtained between 2D and 3D simulations. Moreover, he underlined that more than twenty percent of errors exist between CFD simulations and experiments in the prediction of spray angle.

1.3 Inlet Design of Pressure Swirl Atomizers

The inlet geometry of the PSA determines its performance characteristics and design strategy. Circular and rectangular ports are widely used in industry. The circular ports are easier to manufacture than rectangular ports. However, in the circular ports,

controlling the rate of supplied angular momentum is challenging. Because port dimensions change in axial and tangential directions with the increasing diameter of the port. Change in dimension toward tangential direction determines the swirl arm of the flow. Thus, radial and angular momentum depend on each other in a specific number of ports. The number of inlets has to be changed to control angular momentum by keeping radial momentum constant. The rate of angular momentum at the inlet of PSA is critical to control spray angle and stability in the internal flow of PSA. On the other hand, rectangular port dimensions can be changed independently toward axial and tangential directions. Therefore, radial momentum can be changed by keeping angular momentum constant at the inlet, keeping the width of the port constant, and changing the height of the port. In both port types, separating flow inside the inlet evolves as shown in figure 1.1. Because the tangential velocity component of the flow at the inlet is given immediately. The helical inlet is used to eliminate separating flow in the inlet of PSA [14]. The curvilinear geometry of the helix enables the smooth increase of tangential velocity.

Figure 1.1: *Line integral convolution representation of cylindrical port inlets shows separating flow in inlet ports.*

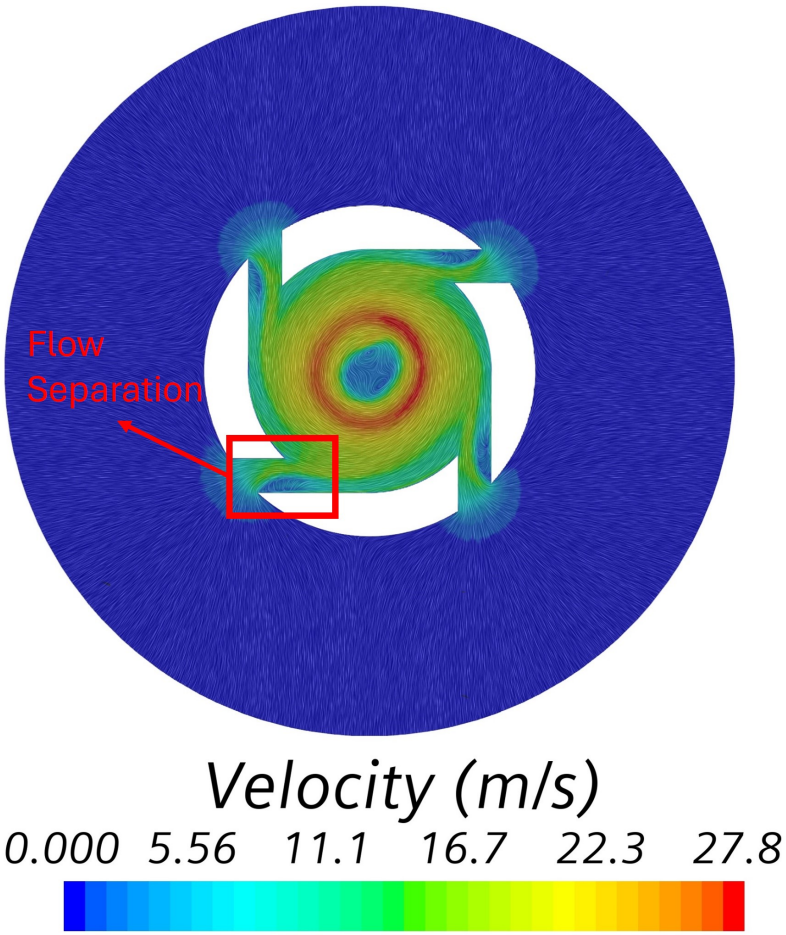

1.4 Formation of Görtler Vortices

In concave walls, laminar to turbulent transition indicates a different behavior than flat plates due to the effect of centrifugal force. In a convex wall, centrifugal force shows stable behavior while the de-stabilizing effect is exerted in the concave wall [15]. Taylor-Görtler vortex is formed in the flow on the concave wall, which is a three-dimensional disturbance in the flow. Due to this vortex form, boundary layer transition evolves earlier than the flat plate. Görtler [16] conducted a stability investigation based on the time-dependent eigenvalue problem for laminar boundary layers on concave walls and concluded that streamwise-oriented vortex structures occur when the Görtler number passes critical value. Görtler number given in equation (1.1) is a combination of Reynolds number based on momentum thickness of boundary layer t_m, free stream velocity V_{free} and ratio of the momentum thickness to radius curvature of concave surface R_c.

$$G = \frac{V_{\text{free}} t_m}{\nu} \times \sqrt{\frac{t_m}{R_{\text{c}}}} \tag{1.1}$$

Liepmann [17] has conducted an experimental study in the flow on concave, flat, and convex walls to understand the effect of Taylar-Görtler vortices on concave walls. He reports that turbulence transition occurs further in convex walls than in concave walls. He also investigated the effect of background turbulence in laminar to turbulent transition on the concave walls. He reported that the critical Görtler number for transition varies between 4 and 10 with varying background turbulence levels.

1.5 Open Questions in the Literature

Open questions in literature are as follows,

- Does Görtler Vortices occur in two-phase swirling film flow?
- How can the initiation of Görtler vortices be determined in two-phase swirling film flow?

- Without separation near the inlet of open-end PSA can Görtler vortices occur in liquid film?
- How does the internal flow and spray film of PSA behave without jet-jet interaction of inlets?
- When identical inlet conditions are provided in 2D axisymmetric and 3D simulations of an open-end PSA, can the results of 2D axisymmetric simulations be overlapped with the 3D simulations?
- How should the inlet geometry of the PSA be designed to ensure uniform flow at the inlet?

1.6 Objective of the Study

The present work aims to investigate the formation of three-dimensional (3-D) flow structures and their impact on the performance of pressure swirl atomizers (PSAs) in comparison to two-dimensional (2-D) axisymmetric flow simulations. To achieve this, identical ring-like inlet conditions are applied in both the 2-D axisymmetric and 3-D simulations, which helps to eliminate any inlet-inlet interaction that could occur when a finite number of inlet ports are used. This comparison can potentially demonstrate the predictive capabilities of 2-D axisymmetric simulations. An open-end PSA geometry is employed to avoid additional disturbances that may arise from a converging swirl chamber geometry. Görtler vortices are observed in the 3-D simulation, as expected. The formation of these vortices seems to initiate with flow separation occurring next to the inlet. An additional simulation, which included an axial swirling film flow inlet condition, indicated that Görtler vortices could develop even without flow separation. In the scope of the analysis results of Görtler vortex formation and its effect on performance parameter prediction capability of 2-D axisymmetric simulations, a blade inlet geometry is designed

for open-end PSA to achieve similar inlet conditions with continuous ring-like inlet. With the blade inlet geometry, 2-D axisymmetric simulations have the potential to predict the performance parameters of PSA accurately.

1.7 Hypothesis of the Study

In the literature, the validity of 2-D axisymmetric simulations in predicting PSA performance parameters has been studied. However, these studies were carried out by converting the conditions of conventional finite-number of port inlets into continuous inlets in 2-D axisymmetric simulations. It has been reported in the literature that finite-number inlets have jet-jet interaction, and they create three-dimensional structures in the internal flow of PSA and result in non-uniform spray distribution. The comparison between 2-D axisymmetric and 3-D PSA simulations should be compared in identical continuous inlet conditions, and it should be investigated whether the flow produces three-dimensional structures by itself in 3D simulation and whether uniform flow patterns can be achieved with an ideal continuous inlet should be observed. In the scope of comparison results, an inlet geometry can be designed that minimizes or eliminates the strength of 3-D structures and enables accurate prediction of PSA performance parameters by using 2-D axisymmetric CFD simulations.

1.8 Methodology

High-fidelity flow simulations of a three-dimensional (3-D) open-end PSA with a continuous ring-like axisymmetric inlet surface were conducted. Swirling two-phase flow is captured with the VOF method and a second-order direct solution of the incompressible Navier-Stokes equations, which is called Quasi Direct Numerical Simulations (Quasi-DNS).To avoid flow separation in the injector, the open-end type PSA is selected for the study, as separation can be expected downstream of a close-end PSA contraction.

Three-dimensional flow structures are searched in the flow field, and they are visualized by utilizing the iso-surface and streamlined post-processing method. The impact of these structures on predictive capabilities of 2-D axisymmetric simulations for PSA performance parameters are analyzed over instantaneous and averaged velocity distribution, pressure drop, film thickness, spray angle, and the shape of the film emitted from the orifice.

The blade inlet is designed by conducting 3-D VOF blade inlet simulations. In simulations, flow in blade inlet and %40 of PSA nozzle is solved. Viscous loss and inlet flow angle are extracted from these simulations. The inlet flow angle and viscous pressure loss were determined through the blade inlet simulations. The calculated inlet flow angle was applied as the inlet boundary condition in 2-D axisymmetric simulations. The total pressure loss of the blade inlet PSA was computed by adding the viscous pressure loss obtained from the blade inlet simulation to the pressure drop calculated from the 2-D simulation. The validity of the 2-D simulations for blade inlet PSA on performance parameters is examined by comparing the spray angle and pressure drop with the experimental results.

2. EXPERIMENTAL SETUP

Tap water is used in the pressure and volume flowrate measurements of blade inlet PSA conducted in the experiments. The gauge pressure is measured with ABB PGS100 model pressure transducer with %0.25 accuracy within the 0-40 bar range. The electromagnetic flow meter ABB Processmaster 630 model is used in volume flowrate measurements with %0.4 accuracies, and the PT100 temperature sensor is used in temperature measurements. The water is pressurized with an axial piston pump, and the pump is fed with a centrifugal pump. The flow rate is adjusted with the help of a Gate valve. The flow is conditioned to $24^{\circ} \pm 2$ with a thermostat system with a 3kW resistance heater. Data measured from the sensors are collected by the NI CRIO 9066 data acquisition (DAQ) system. The set-up schematic is shown in figure 2.1. In pressure drop measurements, the pressure drop of the flow line is determined by conducting flow rate-pressure measurements without a nozzle. Secondly, the measurements are carried out with a nozzle. The pressure drop of the nozzle is determined by subtracting the first measurement from the second. In the data processing procedure, data is collected with and without flow. Then, the collected data is filtered with a Gaussian distribution filter and averaged in time. The final result is computed by subtracting collected data with flow from those without flow.

Figure 2.1: *Schematic diagram of the experimental set-up.*

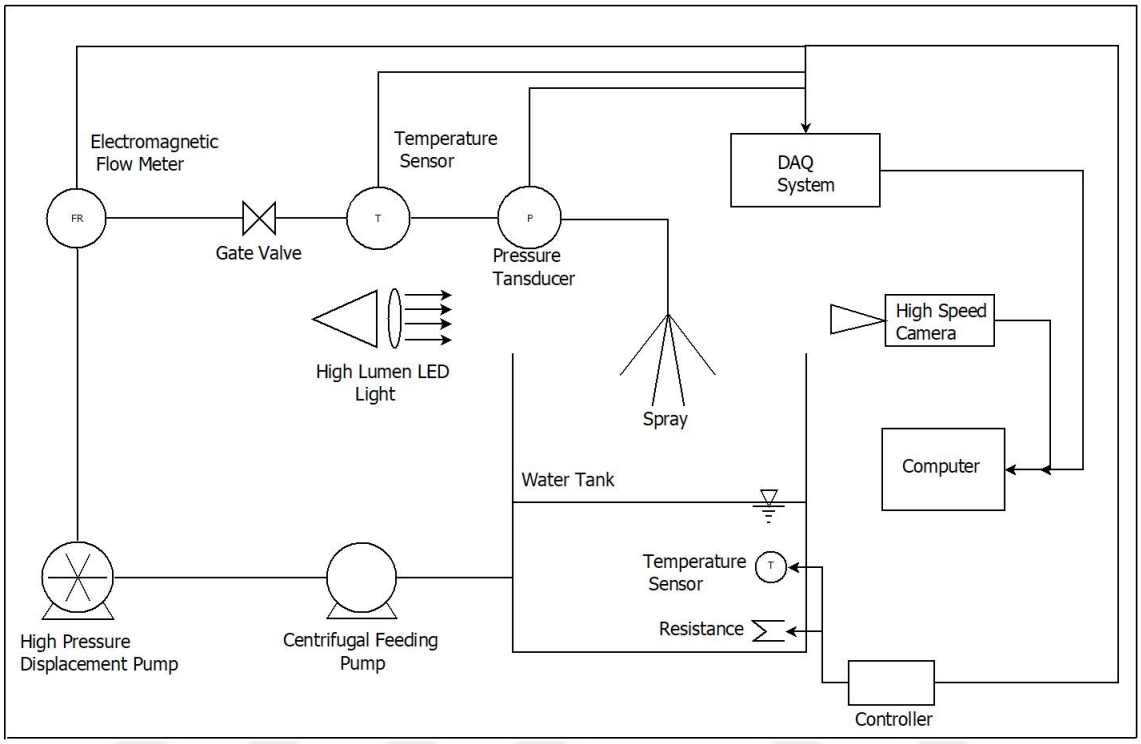

High-speed images are obtained from a Photron Nova S6 high-speed camera using the shadowgraph method to measure the spray angle and observe the film flow. 105W high-lumen COB LED is used as a light source. The images are obtained at 6400 frames per second (FPS) and 21×10^{-9} second shutter speed. In the computation of spray angle, 1600 spray images are taken. Then, the standard deviation of the images was computed and subtracted from the mean background image, shown in figure 2.2. The maximum standard deviation points for the right and left spray film are determined in each horizontal line of the image. Finally, the linear function is fitted to the determined points, and the spray angle is computed from the function slope.

Figure 2.2: *Standard deviation image subtracted by the mean background image. The red line represents the maximum standard deviation point. The green-blue dashed line is the selected section for spray angle computation.*

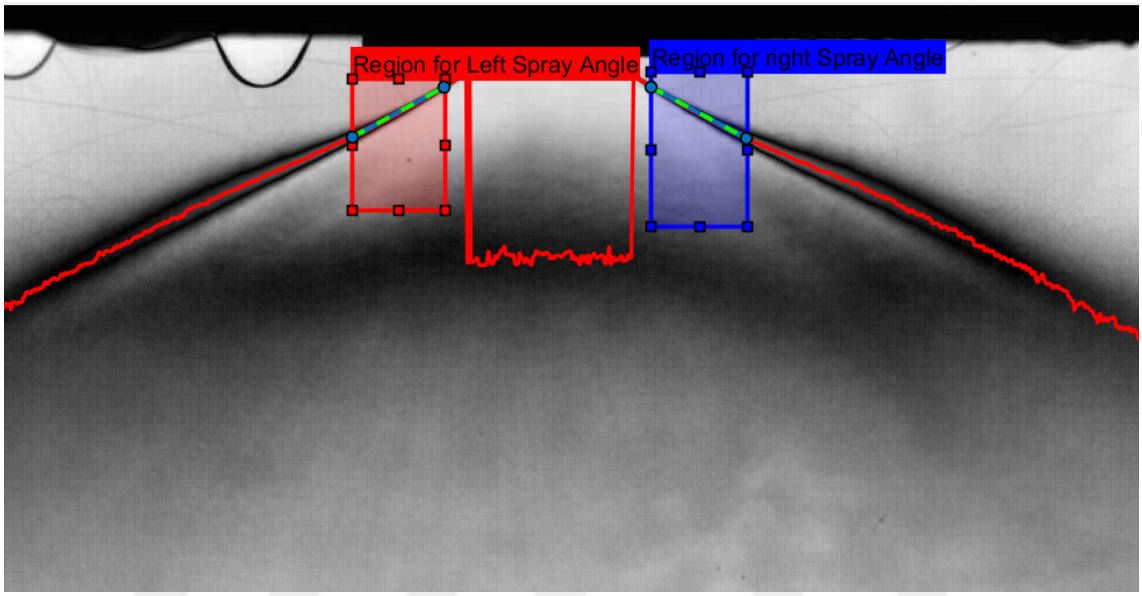

The blade inlet PSA is designed in two parts: the main nozzle and its cap are shown in figure 2.3. In this way, the nozzle can be manufactured using the milling method. The main part of the nozzle is manufactured from 316 stainless steel, and copper is used for its cap. Combining copper and stainless steel as hard and soft metals in the assembly, metal-to-metal sealing is aimed between the main nozzle and its cap. The parts are mounted by using four screws which equidistant from each other to enable homogeneous compression on the sealing area.

Figure 2.3: *Design of blade inlet atomizer.*

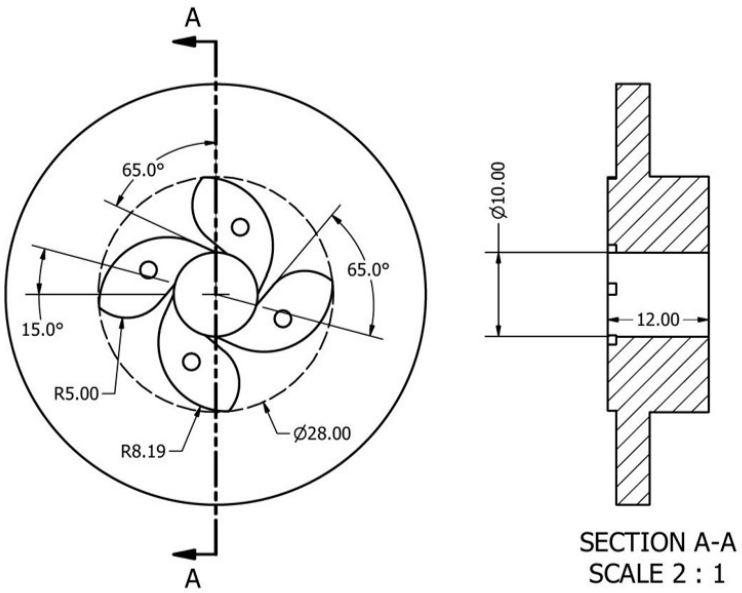

(a) Geometric dimensions specifications.

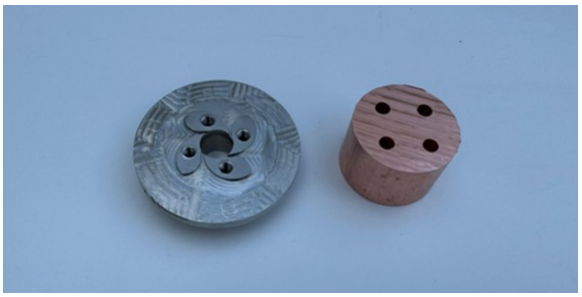

(b) Parts of blade inlet atomizer.

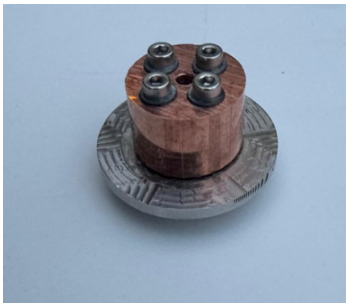

(c) Assembly of the atomizer.

3. COMPUTATIONAL METHODOLOGY

3.1 Governing Equations

The finite volume method is used in Simcenter Star-CCM+ for Newtonian fluids. Hence, the integral form of the continuity and momentum equations in 3.1 and 3.2 are applied to each cell in the computational domain.

$$\frac{\partial}{\partial t}\int_V \rho dV + \oint_A \rho \mathbf{U}\cdot\mathbf{n} d\mathbf{A} = \int_V S_u dV \tag{3.1}$$

$$\frac{\partial}{\partial t}\int \rho\mathbf{U}\, dV + \oint \rho\mathbf{U}\otimes\mathbf{U}\cdot\mathbf{n}\, dA = -\oint P\mathbf{n}\, dA + \oint \mu\nabla\mathbf{U}\cdot\mathbf{n}\, dA + \int f_s\, dV + \int f_b\, dV \tag{3.2}$$

where $\mathbf{U}$,P, ρ, and μ are the velocity vector, pressure, density and dynamic viscosity of the fluid, respectively. f_s is the surface tension force in this study. The mass source term (S_u) is omitted due to the absence of any mass source. The gravitational force is also negligible due to the relatively high inertia of the flow. Therefore, the body force term (f_b) is also omitted.

The volume fractions of the phases α are tracked by solving the transport equation for the volume fraction in equation 3.3. In a two-phase flow, the transport is solved for the primary phase, which is water in this study, the volume fraction of the secondary phase (air) is calculated as the sum of fractions equal to one.

$$\frac{d}{dt}\int_V \alpha_i\, dV + \int_A \alpha_i\mathbf{U}\cdot\mathbf{n} dA = \int_V \left(s_{\alpha_i} - \frac{\alpha_i}{\rho_i}\frac{D\rho_i}{Dt}\right) dV \tag{3.3}$$

In the VOF method interface between phases represented as mesh cell[7], the viscosity and density are computed by averaging the properties of phases according to the volume fraction of the two given in the equations 3.4 and 3.5.

$$\rho = \sum_i \rho_i\alpha_i \tag{3.4}$$

$$\mu = \sum_i \mu_i \alpha_i \tag{3.5}$$

In cells without an interface, the physical properties of the individual phases are utilized. When the discretization is sufficiently small, it is expected that the interface will be represented by a single cell aligned with the normal vector of the interface. This cell will possess the weighted fluid properties of the immiscible phases. However, if the discretization is not fine enough, numerical diffusion errors may occur. In addition to the cell size, the time step also needs to be adjusted to a small enough value to eliminate these diffusion errors.

The CSF model accounts for the surface tension force, denoted as $(\mathbf{f_s})$. This force is determined by the surface curvature (κ_s) and the normal vector $(\mathbf{n}^*)$ at the interface as follows:

$$\mathbf{f_s} = \sigma \kappa_s \nabla \alpha \tag{3.6}$$

where σ is the surface tension and

$$\kappa_s = -\nabla \cdot \mathbf{n}^* \tag{3.7}$$

The normal vector is calculated based on the gradient of the volume fraction of the phases within the CSF model.

$$\mathbf{n}^* = \frac{\nabla \alpha}{|\nabla \alpha|} \tag{3.8}$$

3.2 Model Set-Up

2-D axisymmetric and 3-D Görtler vortex simulations was performed at Re_{bulk} = 3582 and 7163. For the blade inlet PSA simulations, Re_{bulk} varies between 13,683 and 23,357. The Reynolds numbers are kept low so that high fidelity solution of governing equations without any turbulence model(also called quasi-DNS) represents the flow accurately [18]. The flow is assumed to be immiscible, two-phase, incompressible, and

transient. The multiphase nature of the flow is captured with the VOF method. The computational domains are shown in the figures 3.1 and 3.2. Simulation cases are given in table 3.1. Accordingly, 2-D axisymmetric and 3-D ring-like inlet cases have identical inlet conditions and bulk Reynolds numbers. The 3-D axial inlet case is simulated to compare with the ring-like inlet cases.

Table 3.1: *Simulation cases.*

Simulation Case	**Mass flow rate [g/s]**	$Re_{\textbf{bulk}}$	**Nozzle length** (L) **[mm]**	**Nozzle diameter** (D) **[mm]**	**Inlet length** (L_I) **[mm]**	**Inlet flow angle** (θ_f) **[°]**	**Number of cells**	**Average wall y+**
2-D ring-like inlet	2.5	3582	2	1.0	0.2	63.5	63,311	1.28
	5.0	7163						
3-D ring-like inlet	2.5	3582	2	1.0	0.2	63.5	36,551,949	1.61
	5.0	7163						
3-D axial inlet	5.0	7163	1.435	1.0	-	-	31,196,294	1.45
3-D blade inlet	99.7-166	13683-23358	-	10	-	-	5,033,270	1.28
2-D blade inlet PSA	99.7-166	13683-23358	12	10	0.1667	64.2-64.4	165,830	3.26

Figure 3.1: *Görtler vortex simulation flow domains.*

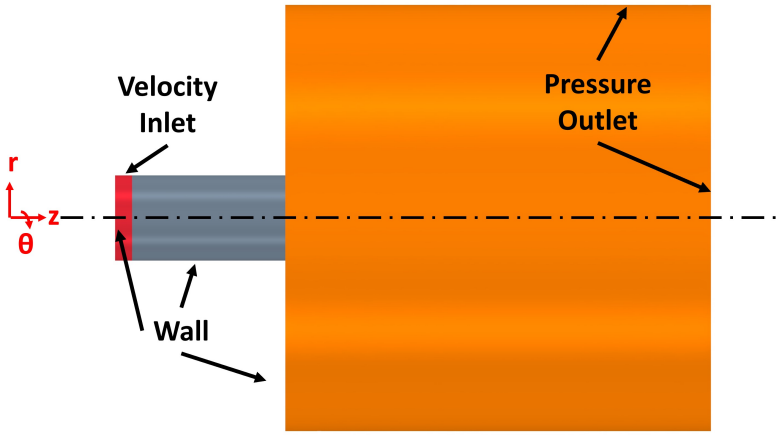

(a) For Görtler vortices Simulations.

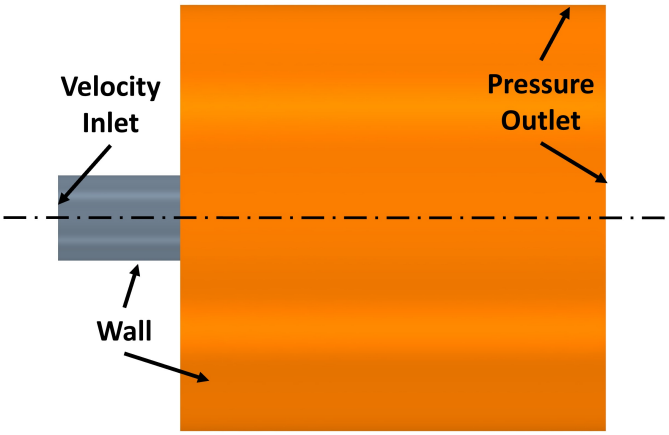

(b) 3-D axial inlet

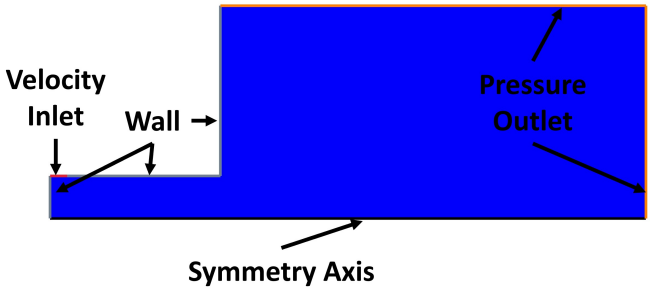

(c) 2-D axisymmetric ring-like inlet

Figure 3.2: *Görtler vortex simulations flow domains.*

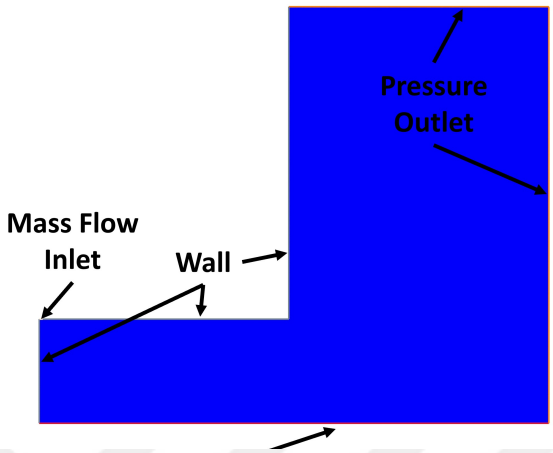

(a) 2-D blade inlet PSA.

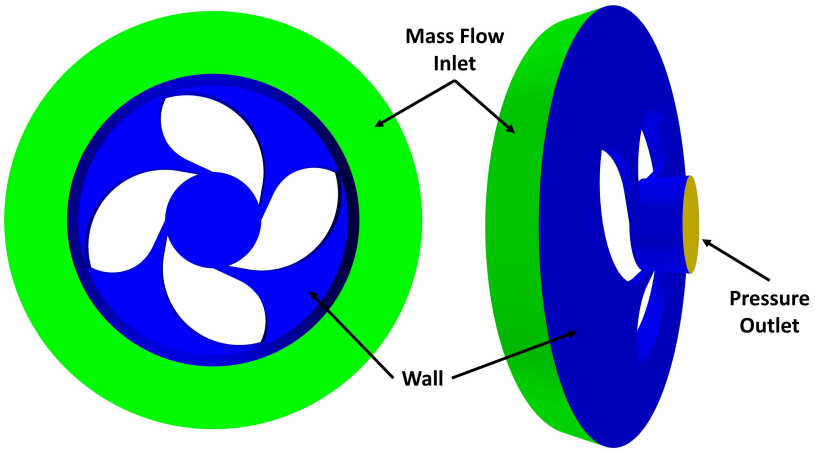

(b) 3-D blade inlet

Governing equations are solved directly by using a SIMPLE scheme. The Gauss-Seidel relaxation scheme is used to solve the discretization matrix. The VOF method is solved with a second-order accurate high-resolution interface capturing (HRIC) scheme. In that scheme, the sharpening factor is set to 0 to minimize artificial compression in the liquid interface. An adaptive time step is used in the model. The time step is computed

according to the convective Courant Number set at 1. The surface tension coefficient σ is set at 0.072 N/m in the CSF model. The identical inlet conditions are used in the simulations. In 3-D ring-like inlet simulation, fluid is fed from the ring-like surface, which is an extended version in the tangential direction of the line inlet in 2-D simulation. In 2-D and 3-D ring-like inlet simulations, the liquid fed to the domains with tangential and radial velocity components is shown in figure 3.3. The flow direction at the inlet kept constant θ_f = 63.5° for all cases. In 3-D axial inlet simulation, the flow field of ring-like inlet simulation liquid film where $z/D = 0.28$ is used. The tangential, axial velocity field and volume fraction of the liquid film of 3-D ring-like inlet simulation are averaged in time, and tangential direction. The average velocity profiles and volume fraction are given as inlet conditions in the 3-D axial simulation shown in figure 3.4.

Figure 3.3: *Inlet conditions of 3-D and 2-D axisymmetric ring-like inlet simulations.*

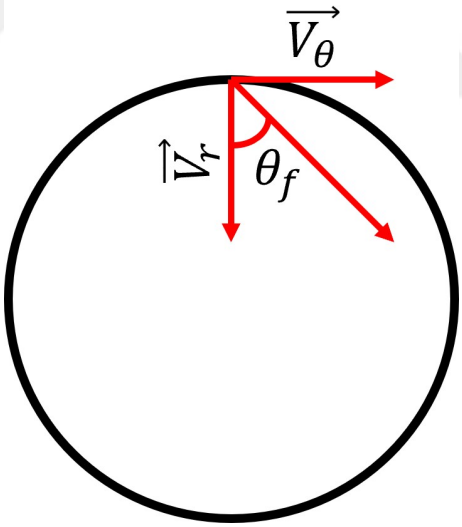

Figure 3.4: *Inlet conditions of the axial inlet simulation.α is the volume fraction of liquid.*

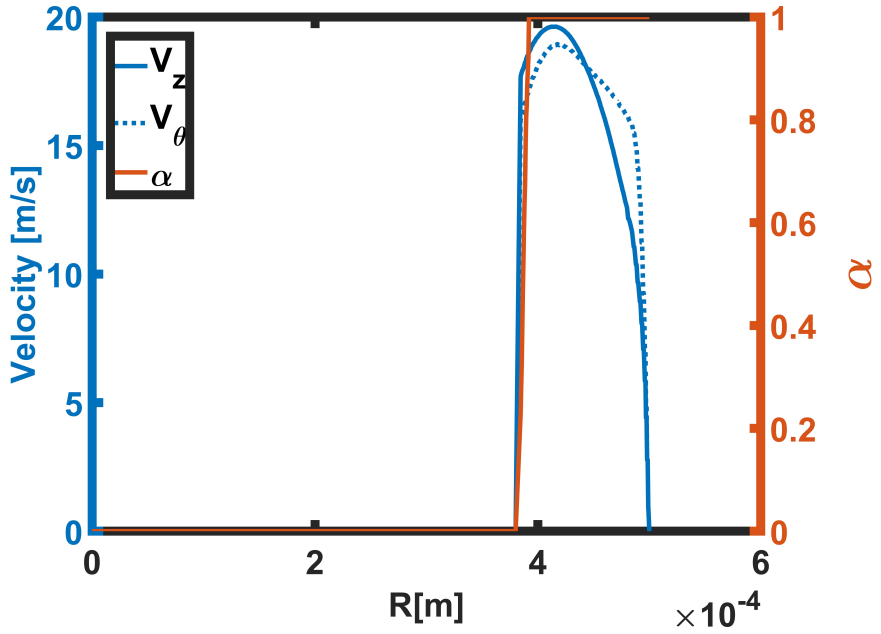

3.3 Grid Sensitivity Analysis

Unstructured polyhedral grids are prepared for the 2-D and 3-D domains, as shown in figures 3.5 and 3.6. Wall y+ values for highest Re_{bulk} numbers for each simulation case are kept lower than 5. To capture spray formation in the near field of the atomizer and the liquid film inside the atomizer, mesh density has increased through the liquid path. Identical mesh parameters are used for 3-D and 2-D axisymmetric Görtler vortex simulation domains. Thus, a grid sensitivity test is performed only for the 2-D domain. The test is based on the thickness of the film. In the 2-D axisymmetric blade inlet, PSA simulations grid sensitivity test is also performed based on film thickness. This parameter is essential for PSA design since it determines spray formation and correlates with droplet size. The accurate solution of the momentum equation relies on precisely predicting the interface between different phases. In the Volume of Fluid (VOF) method, there isn't a distinct liquid interface that occupies a single mesh cell. Smaller mesh sizes around the interface allow for a more accurate capture of its location. Therefore, a mesh sensitivity test is conducted on the thickness of the liquid film in the Phase Separation Analysis (PSA) since the thickness of the liquid film is directly influenced by the geometry of the interface.

Figure 3.5: *Görtler vortex simulations grid configurations.*

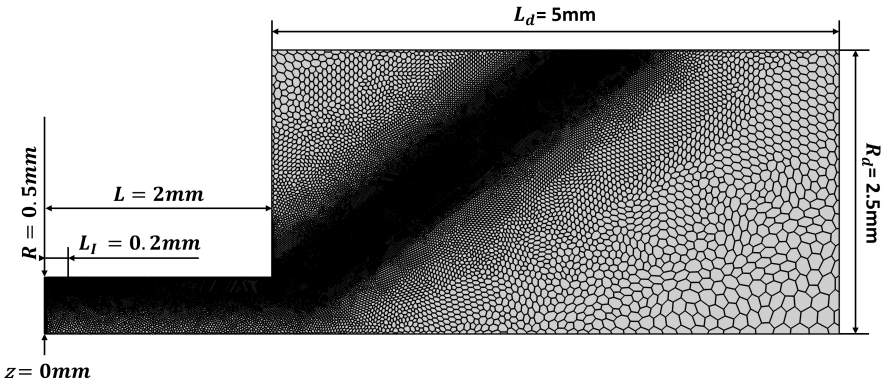

(a) For Görtler vortices Simulations.

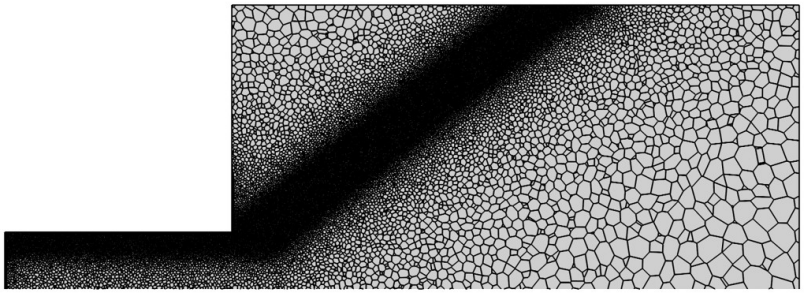

(b) 3-D axial inlet

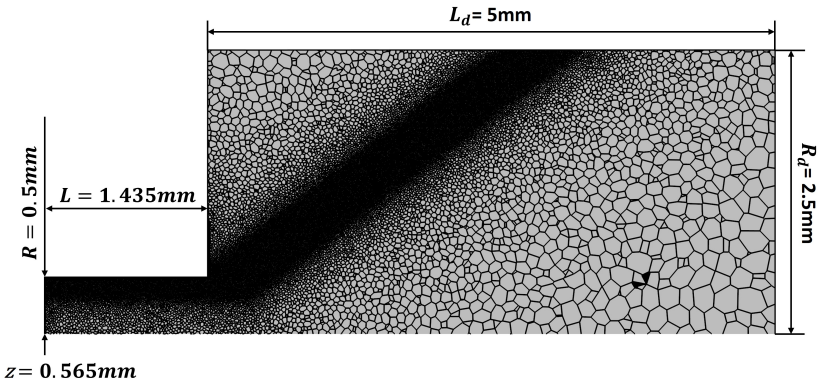

(c) 2-D axisymmetric ring-like inlet

Figure 3.6: *Blade inlet PSA simulations grid configuration.*

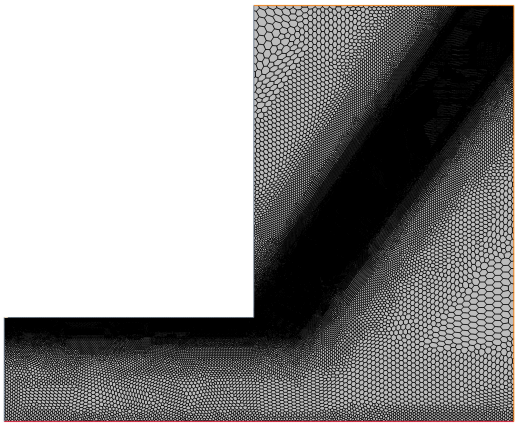

(a) 2-D Blade inlet PSA

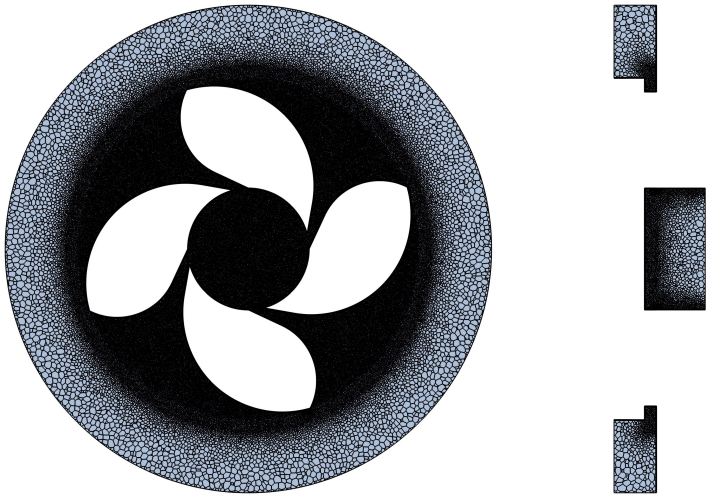

(b) 3-D Blade inlet

The results of the grid sensitivity test shown in figure 3.7 indicate that the film thickness converges after the cell count is 0.6×10^5 and for the blade inlet PSA simulation

film thickness converges after 30 thousand cell element. In the Görtler vortex simulations, the number of cells is selected as 63311 for the blade inlet PSA simulations 165830. The ratio of film thickness with respect to office radius in Görtler vortex simulations is rather higher than in blade inlet PSA simulations. Therefore, in the Görtler vortex simulations, the number of elements is selected just after the film thickness is converged in the grid sensitivity because the film is thick enough to observe spray film. However, in the blade inlet and PSA simulations, the film is quite thin with respect to the radius of the orifice. Thus, more grid elements are selected after convergence of grid sensitivity analysis in blade inlet PSA.

Figure 3.7: *Grid sensitivity studies based on the film thickness(t_f). The film thickness is normalized by the radius of the orifice.*

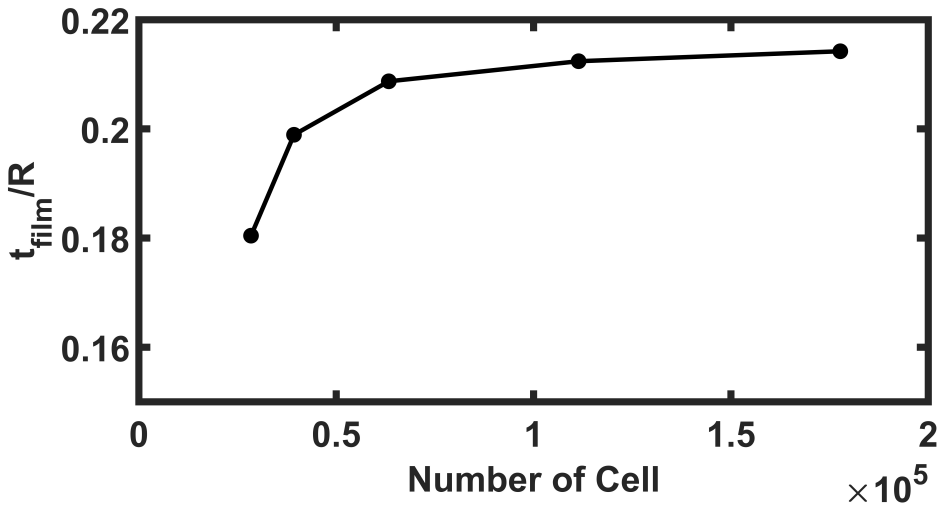

(a) For Görtler vortices Simulations.

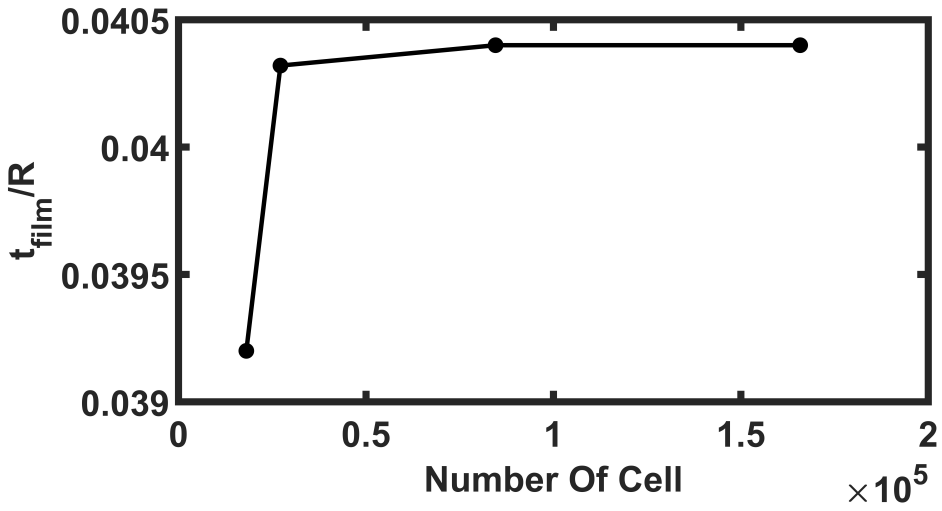

(b) For blade inlet PSA simulations.

In 3-D blade inlet simulations, the grid sensitivity test is performed based on viscous loss in the inlet shown in figure 3.8 because the aim of the simulations is the observation of flow structure in the blades of PSA, and viscous loss is the objective parameter in the simulations. The test results indicate that viscous loss converges after 5×10^6 cell. 5,033,270 cells are used in the discretization of the domain for 3-D blade inlet simulations.

Figure 3.8: *Grid sensitivity study on the basis of viscous loss in blade inlet.*

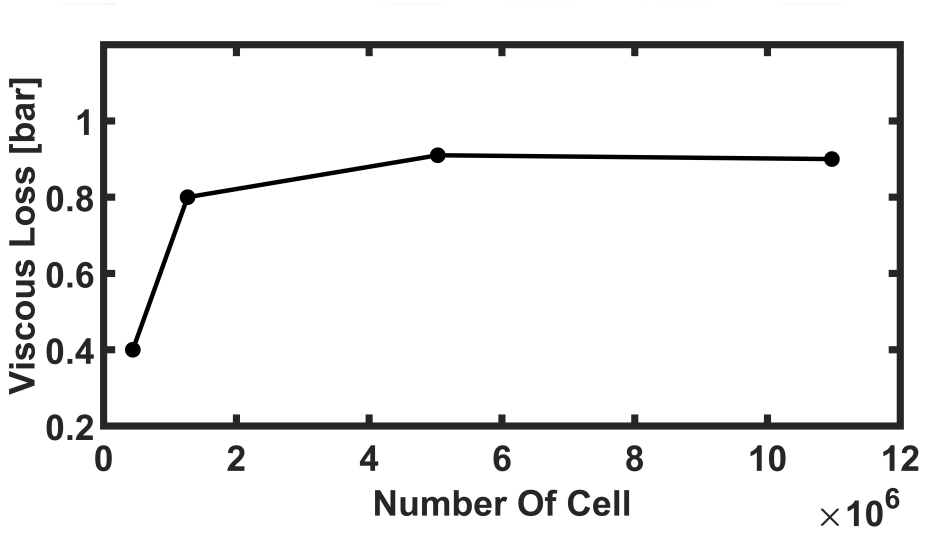

Instantaneous and averaged variable fields like velocity and liquid volume fraction are used for comparisons. For 2-D axisymmetric flow, only time averaging is used, whereas for 3-D simulation, time- and θ- (angular coordinate with respect to the symmetry axis of the PSA) averaging are used. Velocity and volume fraction data in 2- and 3-D time averaged simulation domains are remapped to a structured grid to compare the simulations properly. θ averaging is made during remapping.

3.4 Post Processing

Instantaneous and averaged variable fields like velocity and liquid volume fraction are used for comparisons. For 2-D axisymmetric flow, only time averaging is used, whereas for 3-D simulation, time- and θ- (angular coordinate with respect to the symmetry axis of the PSA) averaging are used. Velocity and volume fraction data in 2- and 3-D time-averaged simulation domains are remapped to a structured grid to compare the simulations properly. θ averaging is made during remapping.

The convergence test is conducted to identify the start of time averaging. The inlet pressure signifies the convergence of the velocity field, while the volume within the domain indicates the liquid volume fraction. The results in figure 3.9 reveal that the liquid volume converges later than the inlet pressure. This convergence of liquid volume is essential for calculating the spray angle, film thickness, and spray film shape. Consequently, the beginning of time averaging is defined based on the convergence of liquid volume within the domain. The averaging period corresponds to three flow-through times, which are determined by dividing the volume flow rate by the liquid volume in the domain.

Figure 3.9: *Liquid volume in the computational domain and inlet static pressure showing the convergence of simulations in time.*

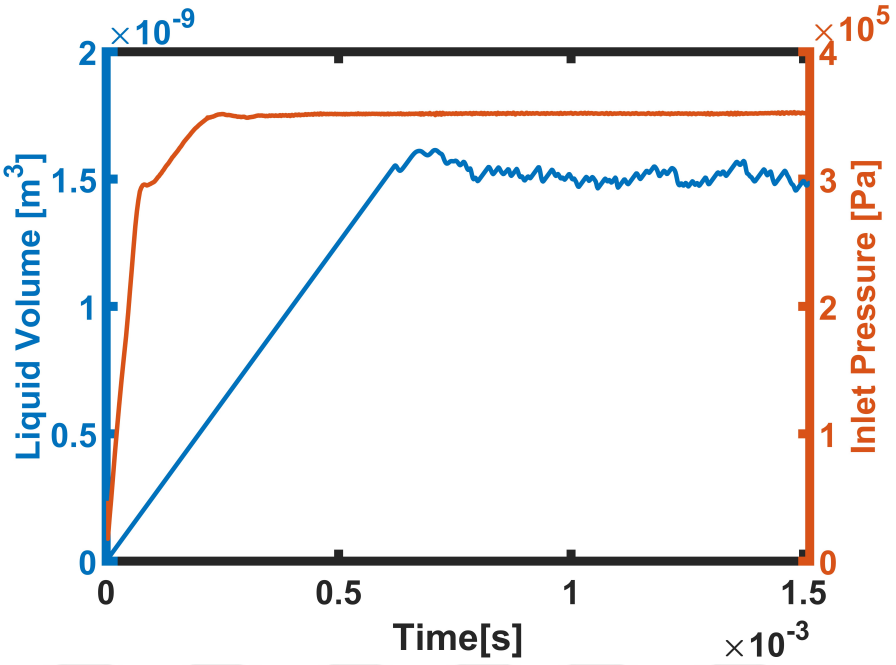

In the remapping process, unstructured polygonal grids are remapped on a structured square grid with a grid size of 1×10^{-5} m. The remapping is performed by using a distance-based weighted averaging shown in equations 3.9 and 3.10. The variable $v^*(r, z)$ represents the value on the structured remapping grid. The simulated domains used for averaging consist of the data points $v(r_i, z_i)$ distributed around the center of the grid point at (r, z) within a circular area of radius r_c in 2-D simulations. For 3-D simulations, $v(r_i, z_i)$ are the data points within a torus that has a minor radius of r_c. The circular axis of the torus is located at the coordinates (r, z). For all simulations, the value of r_c is set to 1×10^{-5} m. The weighted average is calculated using the following equation:

$$v^*(r, z) = \frac{\sum_{i=1}^{N} v(r_i, z_i) w(i)}{\sum_{i=1}^{N} w(i)} \tag{3.9}$$

Here, $w(i)$ is the weight function defined as:

$$w(i) = 1 - \sqrt{\Delta r_i^2 + \Delta z_i^2}/r_c \tag{3.10}$$

In this equation, Δr_i and Δz_i represent the distances from a data point to the grid point at (r, z) on the remapped grid.

4. RESULTS

4.1 Comparison of 2D and 3D Simulations in Terms of PSA Performance Parameters and Velocity Fields

A swirling liquid film forms in the PSA downstream of the inlet, as shown in figure 4.1. To conduct an identical comparison, velocity and volume fraction data in the domain of 3-D simulation is averaged in theta direction, and the data of 2-D simulations are remapped to the same locations using a weighted average. The results from both the 2-D axisymmetric simulations and the 3-D simulations with a ring-like inlet exhibit nearly identical liquid film characteristics. Additionally, the velocity profiles and liquid volume fractions within the atomizer at various cross-sections are compared in the figures 4.2 and 4.3 for two different Reynolds numbers. As observed, the results from the 2-D and 3-D simulations largely overlap, with only a slight difference in the ratio V_θ/V_b near the exit of the atomizer.

Figure 4.1: *Comparison of liquid film extracted from time- and θ- (only for 3-D simulations) averaged volume fraction of liquid for $\alpha > 0.5$.*

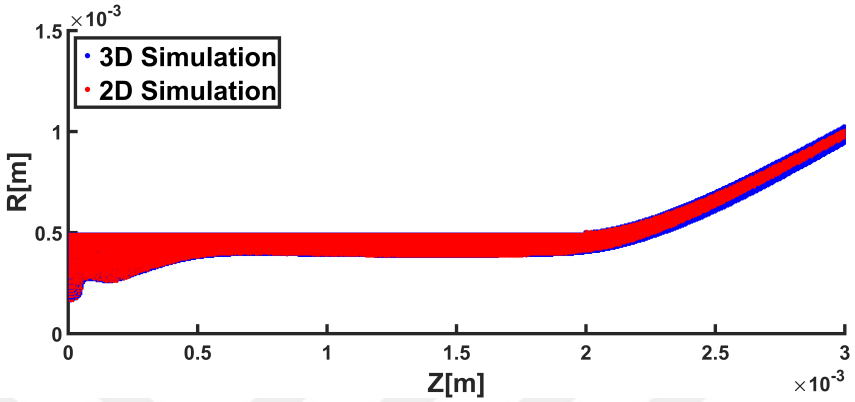

(a) 2-D axisymmetric and 3-D ring-like inlet simulation, Re_{bulk} = 3582

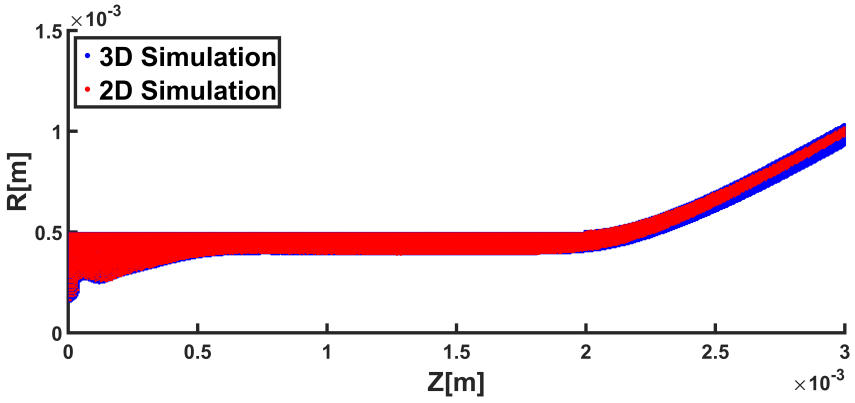

(b) 2-D axisymmetric and 3-D ring-like inlet simulation, Re_{bulk} = 7163

Figure 4.2: *Time- and θ-(only for 3-D simulations) averaged velocity and liquid volume fraction distributions of 2-D and 3-D ring-like inlet simulations along the radial direction at* Re_{bulk} *= 3582.*

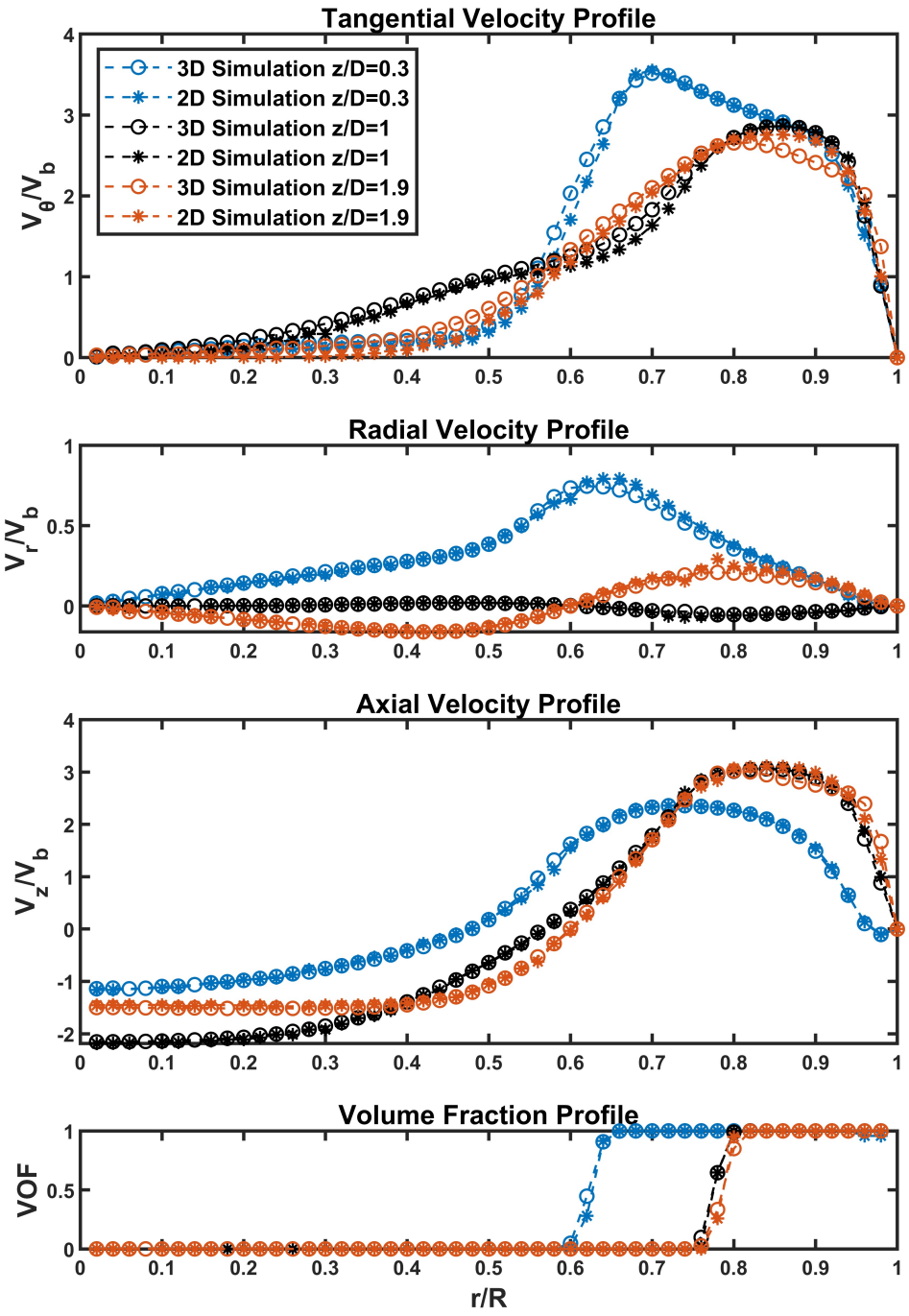

Figure 4.3: *Time- and θ-(only for 3-D simulations) averaged velocity and liquid volume fraction distributions of 2-D and 3-D ring-like inlet simulations along the radial direction at* Re_{bulk} *= 7163.*

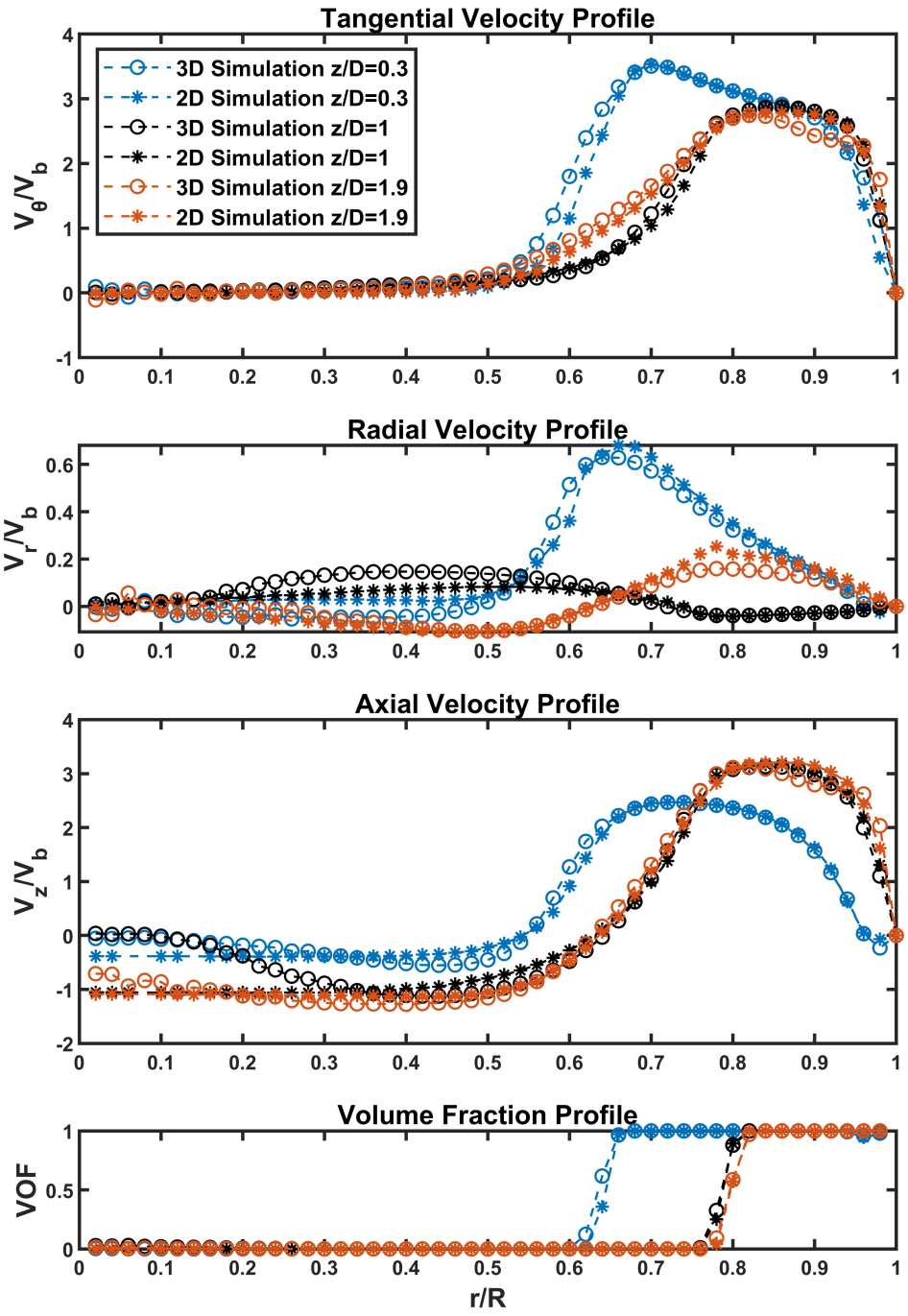

Furthermore, the performance parameters of the 2-D and 3-D atomizers with a ring-like inlet, presented in table 4.1, match almost perfectly. The film thickness and half-spray angle are computed from the averaged data. The film thickness is calculated by averaging the film thickness between $z = 1.0D$ and $z = 1.5D$. In the spray angle computation, the outer interface points of the spray film are obtained from the averaged volume fraction data between $z = 2.5D$ and $z = 3D$. The trend line of the points is drawn by using linear regression. The spray angle is calculated from the slope of the linear trend line. This significant level of alignment across the simulations illustrates that when inlet conditions are identical, the outcomes in both 2-D axisymmetric and 3-D simulations yield nearly identical results.

Table 4.1: *Performance parameters of the atomizer.*

Simulation Case	**Mass Flow [g/s]**	$Re_{\textbf{film}}$	$Re_{\textbf{bulk}}$	**Pressure Drop** (ΔP **[bar])**	**Film Thickness** ($t_{\textbf{film}}$ **[**μ**m])**	**Half Spray Angle [°]**
2-D axisymmetric	2.5	1017	3582	0.559	113	32.7
	5.0	2012	7163	2.242	108	33.3
3-D ring-like inlet	2.5	1017	3582	0.558	113	32.1
	5.0	2012	7163	2.235	105	33.2
3-D axial inlet	5.0	2012	7163	0.195	119	33.7

4.2 Formation of Görtler Vortices in Internal Flow of PSA

The instantaneous velocity vector fields in the 2-D and 3-D ring-like inlet simulations, as well as the wall shear stress distributions on the PSA wall in the 3-D simulations, are illustrated in figure 4.4. This comparison clearly shows that 3-D flow structures are present only in the 3-D simulations and become more pronounced in the wall shear stress distribution. Upon careful examination of the velocity vectors, it is evident that the jet from the inlet causes flow separation downstream. When flow separates, the wall shear stress reaches its minimum. Conversely, when flow reattaches, the wall shear stress increases again. Although the wall shear stress eventually decays, the influence of three-dimensional flow structures becomes increasingly significant. As a result, the wall shear stress rises in conjunction with a banded swirling pattern.

Figure 4.4: *3-D and 2-D axisymmetric ring-like inlet simulations at Re_{bulk} = 3582 and 7163. Instantaneous wall shear stress contours in the 3-D ring-like inlet simulations(a),(b), instantaneous velocity vector contours in the 3-D ring-like inlet simulations (c),(d), and 2-D axisymmetric simulation (e),(f).*

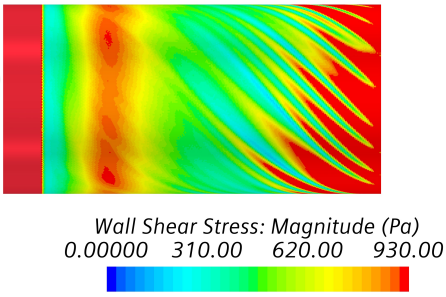

(a) 3D ring-like, Re_{bulk} = 3582

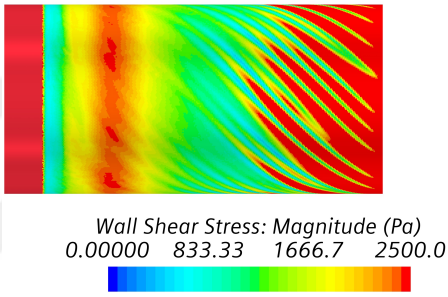

(b) 3D ring-like, Re_{bulk} = 7163

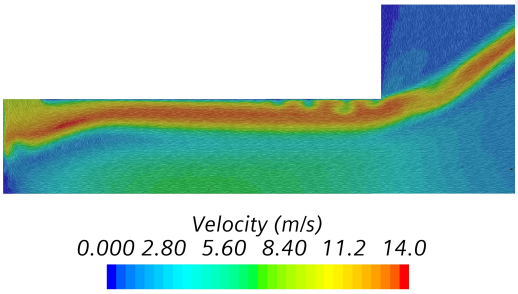

(c) 3D ring-like, Re_{bulk} = 3582

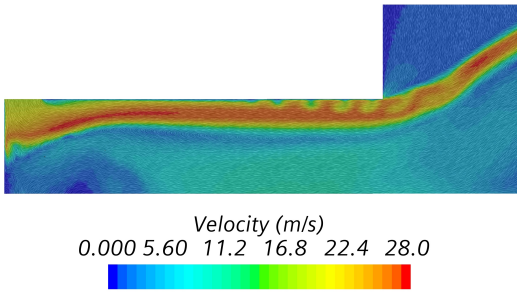

(d) 3D ring-like, Re_{bulk} = 7163

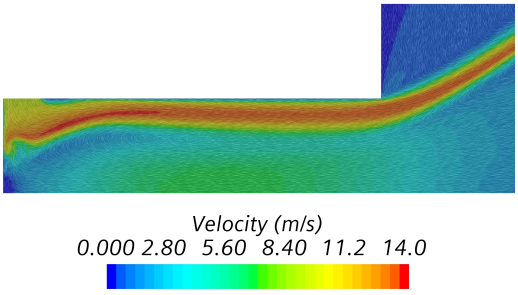

(e) 2D, Re_{bulk} = 3582

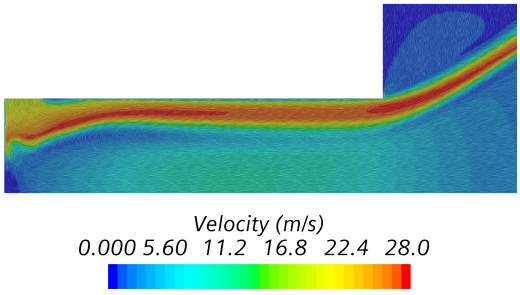

(f) 2D, Re_{bulk} = 7163

While the influence of flow structures on the primary flow characteristics is minimal, they deserve attention for two reasons: they may affect the spray film at the atomizer's exit, and they pique curiosity for their resemblance to Görtler vortices. The former is crucial when the break-up, atomization, spray pattern, and spray uniformity are considered. 3-D simulations with ring-like inlet, velocity, and helicity fields on different cross sections are shown in figure 4.5. Helicity is the scalar product of velocity and vorticity vectors as shown below:

$$H = \int U \cdot \omega \, dV \tag{4.1}$$

This function allows for the interpretation of vortices within the flow. The negative and positive helicity pairs shown in figure 4.5 are correlated with the structures observed in the velocity field. These pairs represent vortices that rotate in opposite directions; however, one of the pairs that rotate in a swirling direction is stronger than the other. This is because the swirling component of the bulk flow increases the kinetic energy of the vortex that is rotating in the same direction as the swirl while it decreases the energy of the vortex rotating in the opposite direction. A similar result is discussed in the study by Vaidya et al. [19], which conducted a numerical analysis of single-phase swirling flow in pipes to investigate vortex structures and their effects on swirl decay.

Figure 4.5: *Instantaneous velocity (a),(b) and helicity fields (c),(d) in 3-D ring-like inlet simulations at Re_{bulk} = 3582 and 7163 on various cross sections where z/D = 1.4, 1.6 and 1.8 perpendicular to PSA axis.*

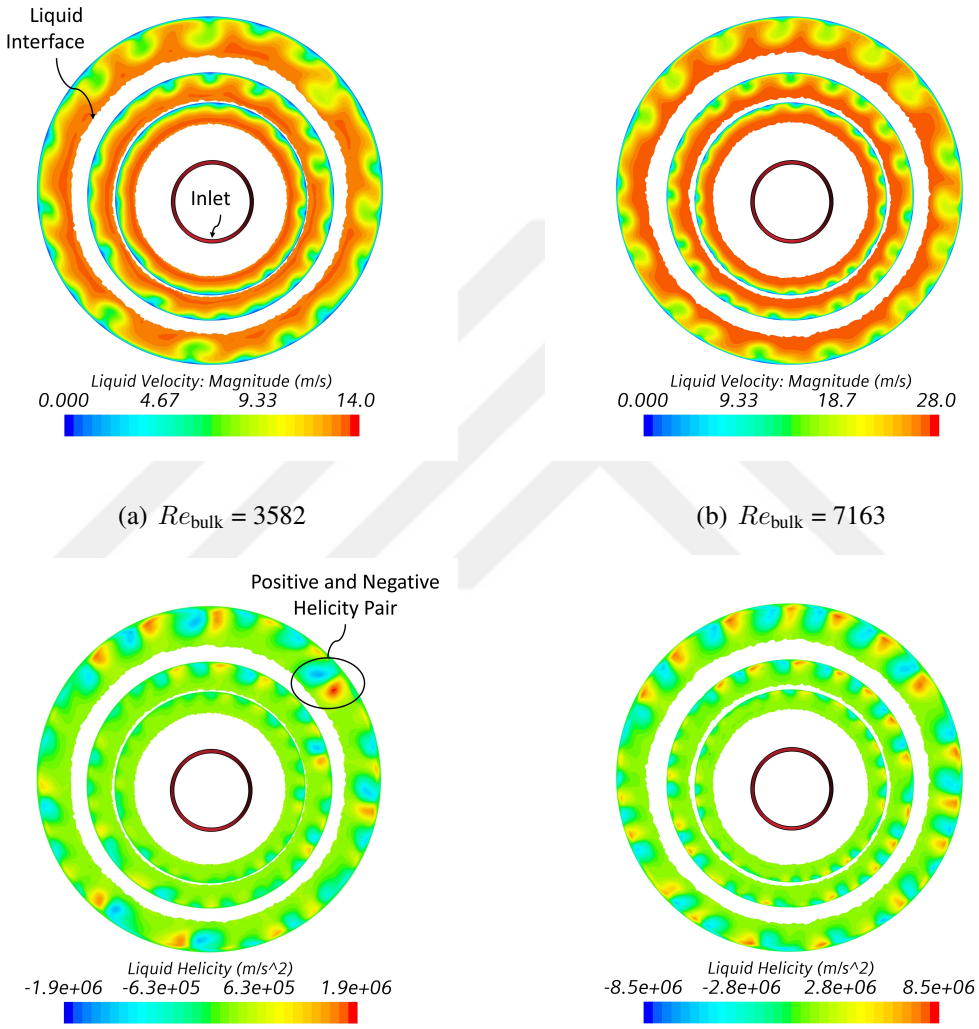

(a) Re_{bulk} = 3582

(b) Re_{bulk} = 7163

(c) Re_{bulk} = 3582

(d) Re_{bulk} = 7163

The observed helicity and velocity structures in the liquid film develop along the helical streamwise direction, as shown in figure 4.6. It was observed that the low-velocity fields are located between pairs of positive and negative helicity structures. Additionally, the number of these structures increases with increasing Re_{bulk}. Based on the observations from the velocity, helicity fields, and isosurfaces of helicity fields, one can conclude that helicity pairs depict Görtler vortices, and low-velocity fields appear due to vortex pairs rotating in opposite directions to each other.

Figure 4.6: *Swirling flow structures in the 3-D ring-like inlet simulations. Visualization is made with iso-surfaces for the low-velocity field (gray), positive helicity (red), and negative helicity (blue) between* $z/D = 1$ *and 1.95. For both low and high Reynolds number simulations, the iso-values are: velocity (gray at 12 m/s and 24 m/s), negative helicity (blue at -5.0 x* 10^5 *m/s*^{2} *and -2.5 x* 10^6 *m/s*^{2}*), and positive helicity (red at 5.0 x* 10^5 *m/s*^{2} *and 2.5 x* 10^6 *m/s*^{2}*).*

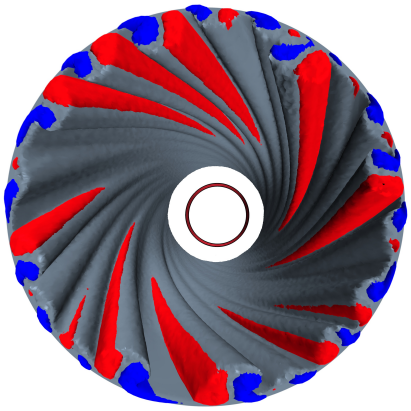

(a) Re_{bulk} = 3582

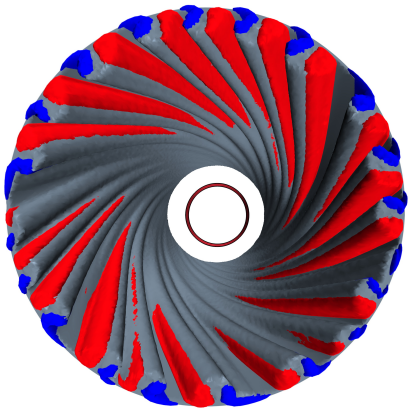

(b) Re_{bulk} = 7163

Görtler vortices are illustrated using streamlines in figure 4.7. These vortices arise from the swirling flow within the PSA, which resembles fluid flow along a concave wall, as suggested by Görtler [16]. The swirling liquid film flow in the PSA follows a helical path. In this helical motion, the flow rotates around an axis, generating centrifugal forces similar to those found in flow over a concave wall. The key difference between these two types of flow is that, in helical motion, the flow also translates in the axial direction. Nevertheless, this axial translation does not prevent the occurrence of centrifugal force, which is the fundamental cause of Görtler vortices.

The small discrepancy between the velocity profiles of 2-D and 3-D ring-like inlet simulations in figures 4.2 and 4.3 can now be explained with the existence Görtler structures in 3-D simulation.

Figure 4.7: *3-D ring-like inlet, instantaneous half-section visualization of Görtler vortices with streamlines seeded on positive helicity iso surface between z/D =1.5 and z/D = 2.*

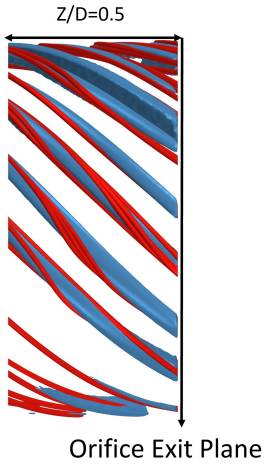

(a) 3D ring-like, Re_{bulk} = 3582

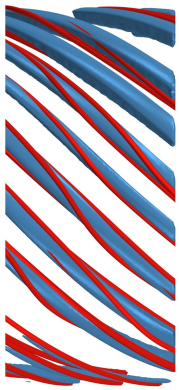

(b) 3D ring-like, Re_{bulk} = 7163

4.3 Computation of Görtler Number

Referring to a free stream flow and a freestream velocity (V_{free}) in the PSA is not possible. Additionally, since the flow follows a helical path, it is necessary to consider the radius of curvature (R_c) based on the helical shape rather than the radius of the PSA. The calculation of momentum thickness (t_m) also requires special attention. To address the absence of a free stream flow, we examine the local shear stress distribution averaged in the tangential direction (see figure 4.8) to establish a reference for the computation of parameters related to the Görtler number. The shear stress plot and distribution shown in figure 4.4 indicate that separation downstream of the inlet diminishes, and the development of the boundary layer begins at the local maximum shear stress. After this point, shear stress begins to decrease, which is also consistent with observations made on a flat plate: maximum shear stress occurs at the leading edge of the flat plate as the boundary layer develops. Therefore, the local maximum of shear stress in the swirling liquid film flow of the PSA is the most appropriate reference point from which to calculate representative values for the free stream velocity and momentum thickness.

Figure 4.8: *θ and time-averaged shear stress plot of 3-D ring-like inlet simulations. Black points present the end of the separation zone.*

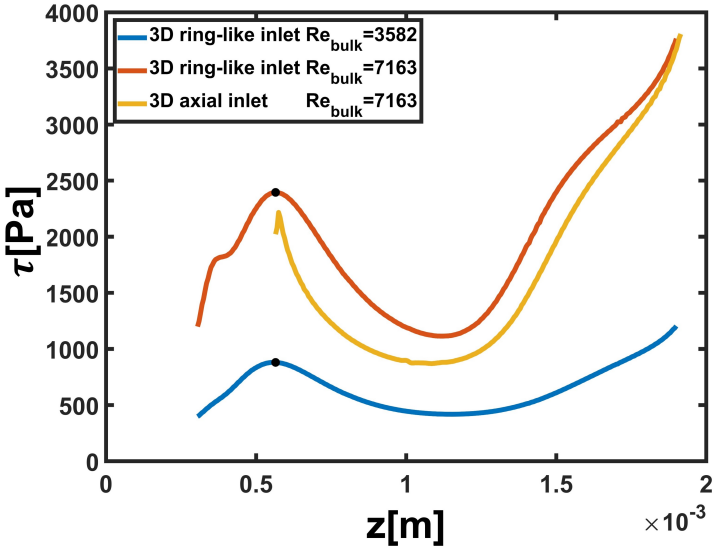

Görtler number (equation. 1.1) includes momentum thickness based on Reynolds number. The numerator part of the Reynolds number consists of the inertial force of the flow. Thus, the square root of the average momentum flow rate flux (P_{flux}) divided by density is used to replace the free stream velocity in the Görtler number. The calculation of average momentum flux is given in equation 4.2.

$$P_{\text{flux}} = \frac{\int_{R-t_{\text{film}}}^{R} \rho V_z (V_z + V_\theta)\, 2\pi r\, dr}{\int_{R-t_{\text{film}}}^{R} 2\pi r\, dr} \tag{4.2}$$

where V_z and V_θ are axial and tangential velocity components at a given plane.

The momentum thickness is a quantity that indicates the proportion of the momentum flow rate of the free stream flow that is converted into drag force. In this study, momentum thickness is computed by calculating the shear force on the wall as follows:

$$t_m = \frac{\int_{z_0}^{z} \int_0^{2\pi} \tau R \, d\theta \, dl}{P_{\text{flux}} \, 2\pi R} \tag{4.3}$$

The geometry of the helical path of the swirling film flow is captured by the helix function written in cylindrical coordinates shown in equation 4.4. Coordinates of points in the helical path are computed as a function of independent variable β in radians, which is the amount of rotation and increase along the helical path. The radial coordinate r of the helix is R_h for a cylindrical helix, and here it is equal to the orifice radius (R). The angular coordinate and axial coordinates of the helix are θ and z, respectively.

$$r(\beta) = R_h = R, \quad \theta(\beta) = \beta, \quad z(\beta) = c\beta \tag{4.4}$$

The pitch of helix (c) is calculated by the ratio of axial velocity V_z to tangential velocity V_θ of the film flow:

$$c = r\frac{V_z}{V_\theta} \tag{4.5}$$

The curvature of the helix (κ_h) is computed by the equation 4.6, and the radius of curvature R_c is the reciprocal of the curvature as shown in equation 4.7.

$$\kappa_h = \frac{r}{r^2 + c^2} \tag{4.6}$$

$$R_c = \frac{1}{\kappa_h} \tag{4.7}$$

Finally, the Görtler number for swirling film flow is formulated as follows:

$$G = \frac{\sqrt{\frac{P_{\text{flux}}}{\rho}} \, t_m}{\nu} \sqrt{\frac{t_m}{R_c}} \tag{4.8}$$

4.4 Onset of Görtler Vortex Instability

Development of Görtler number in axial direction is shown figure 4.9. In this graph, z_0 stands for the location of local maxima of wall shear stress downstream close to the inlet. The calculated Görtler numbers fall within the range observed in Liepmann's

study. Although the Görtler number alone does not show directly the Görtler vortices, in analogy to inferring the transition Reynolds number, we can fairly argue that the observed flow structures in the swirling film are Görtler vortices.

The onset of the Görtler vortex is determined according to the local maxima of the shear stress derivative given in figure 4.10. The initiation of Görtler vortices occurs at a lower Görtler number for $Re_{\text{bulk}} = 7163$ $G \cong 3.6$ compared to $Re_{\text{bulk}} = 3582$ at $G \cong 2.9$. This difference is attributed to the weaker separation near the inlet at $Re_{\text{bulk}} = 3582$. This finding aligns with Liepmann's observation that the transitional Görtler number decreases as background turbulence increases. Moreover, laminar to turbulent transition is followed by monitoring velocity signal in the middle of the liquid film with various points where z/D = 1,1.6,1.9 shown in figure 4.11. The velocity signals indicate that before the evolution of Görtler vortices, sinusoidal velocity signals were obtained where z/D = 1. With the development of Görtler vortices where z/D = 1.6 and 1.9, the signals are randomized. In this case, the source of disturbance arises from flow separation near the inlet, whose impact becomes more pronounced with increasing Reynolds numbers.

Figure 4.9: *Development of Görtler number respect to axial direction. Black points present the beginning of Görtler vortices.*

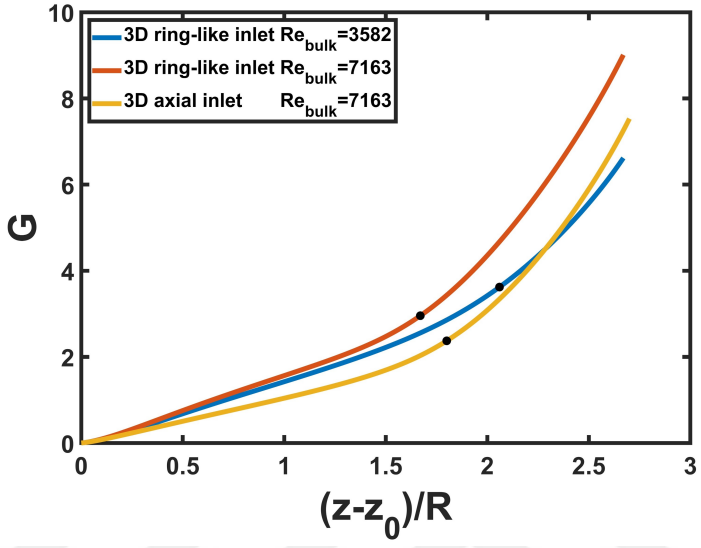

Figure 4.10: *Partial derivative of shear stress in axial direction. Black points present the onset of Görtler vortices.*

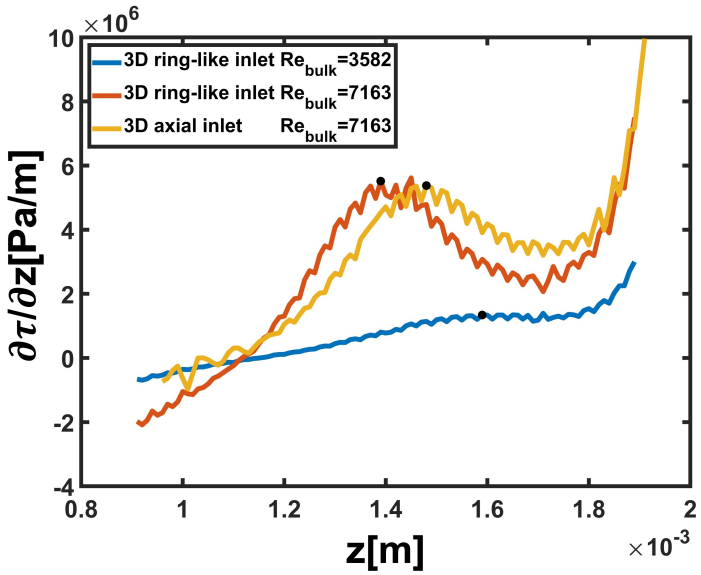

Figure 4.11: *3-D ring-like inlet simulations Re_{bulk} = 7163 velocity signals obtained the same radial position from the middle of the film (r/R = 0.9) and various axial locations where z/D = 1, 1.6, and 1.9.*

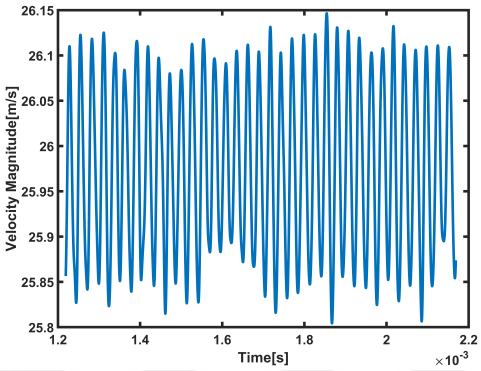

(a) z/D = 1

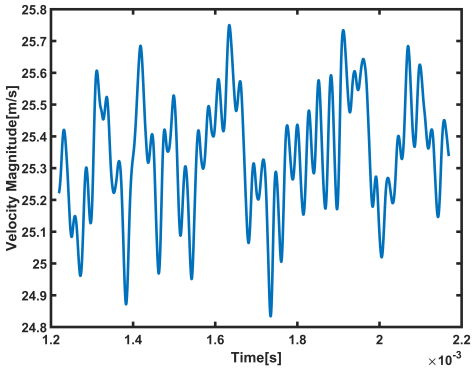

(b) z/D = 1.6

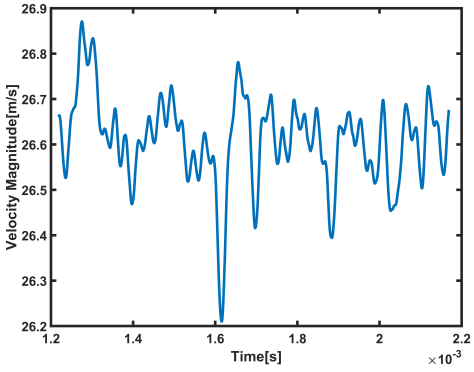

(c) z/D = 1.9

4.5 Effect of Separating Flow on Görtler Vortices

To understand how separation near the inlet affects the generation and development of Görtler vortices, a three-dimensional simulation with an axial inlet is conducted. The inlet conditions consist of time- and θ-averaged axial and tangential velocity profiles in the liquid film and the liquid volume fraction (see figure 3.4). These profiles are extracted from the three-dimensional ring-like inlet simulations at the axial location where the local maximum of shear stress occurs, specifically at $z = 0.000565\,\mathrm{m}$. The radial velocity profile is not given in the axial inlet case to inhibit any instabilities in the liquid film. The results indicate that similar velocity and helicity structures exist in 3-D axial inlet simulation, as shown in figures 4.12 and 4.13. Görtler vortices develop toward the orifice exit as shown in figure 4.14 and figure 4.15. The wall shear stress distribution presented in figure 4.13 clearly shows no signs of flow separation. This evidence demonstrates that Görtler vortices can emerge purely from centrifugal forces, highlighting the capacity for such phenomena to occur without any separation.

As illustrated in figures 4.9 and 4.8, Görtler vortices begin at a Görtler number of $G = 2.46$ in 3-D axial inlet simulations, which is lower than that of the ring-like inlet, and the reduction in wall shear stress is steeper in this case. Due to the lack of radial velocity and its contribution to kinetic energy, the computed shear stresses are lower in the axial inlet simulation compared to the ring-like inlet simulation. As a result, the drag force obtained from integrating these shear stresses, which is used to calculate momentum thickness for the Görtler number, is also lower in the axial inlet than in the ring-like inlet. Furthermore, Görtler vortices in the axial inlet simulation begin to form further downstream with respect to z_0 compared to the ring-like inlet simulation. This indicates that when the disturbance caused by separation is mitigated, the initiation of Görtler vortices is delayed.

Figure 4.12: *Instantaneous velocity (a) and helicity fields (b) in 3-D axial inlet simulation at Re_{bulk} = 7163 on various cross-sections where z/D = 1.4, 1.6 and 1.8 perpendicular to PSA axis.*

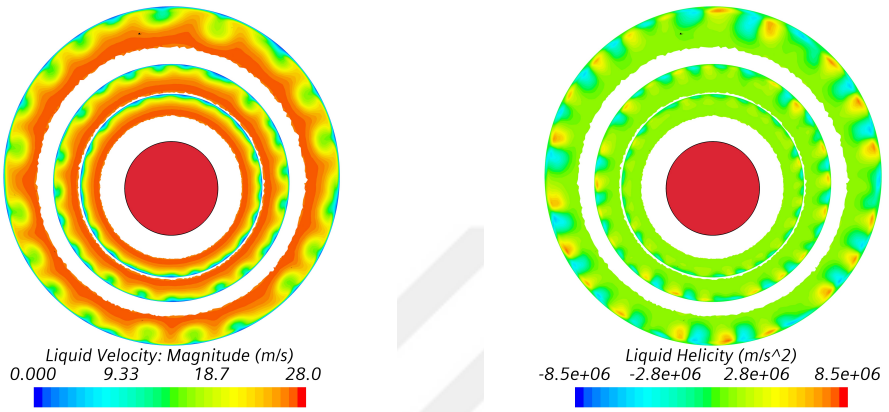

(a) Instant velocity fields

(b) Instant helicity fields

Figure 4.13: *Instantaneous wall shear stress (a) and velocity vector contours (b) in 3-D axial inlet simulations.*

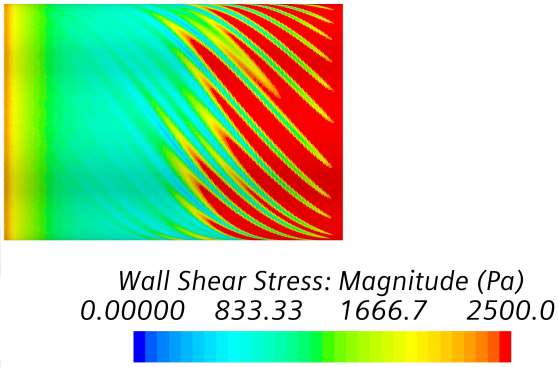

(a) Wall shear stress field on the wall of PSA, Re_{bulk} = 7163

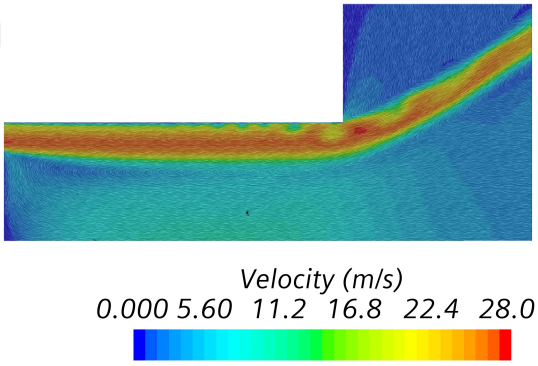

(b) Velocity field in the PSA, Re_{bulk} = 7163

Figure 4.14: *Swirling flow structures in the 3-D axial inlet simulation between $z/D = 1$ and 1.95. Visualization is made with iso-surfaces for the low-velocity field (grey, iso value = 24 m/s), negative helicity (blue, iso value = -2.5 $\times$ 10^6 m/s^2), and positive helicity (red, iso value = 2.5 $\times$ 10^6 m/s^2).*

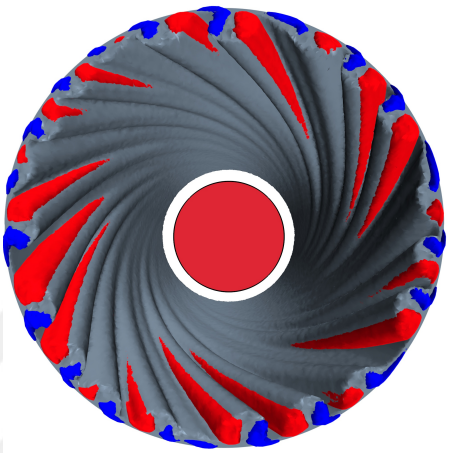

Figure 4.15: *Görtler vortices visualized by the streamlines seeded on positive helicity iso surface between $z/D = 1.5$ and 2 in 3-D axial inlet simulation. The side view of the half-section is shown.*

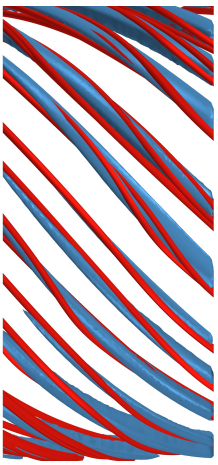

A key finding from the 3-D simulation with an axial inlet is that it yields a pressure drop 10 times lower than that of a ring-like inlet (see table 4.1). In the ring-like setup, fluid enters the PSA's swirling chamber with radial and tangential velocity components. As fluid moves inward, it decelerates radially due to centrifugal force, conserving angular momentum and accelerating axially and tangentially. This process uses much of the pressure potential at the inlet. In contrast, the axial inlet lacks radial velocity components, resulting in no deceleration in that direction and no significant acceleration in axial and tangential directions. Here, the pressure drop is mainly due to viscous dissipation and momentum transfer to the gas phase.

4.6 Effect of Görtler Vortices on Spray Film

The influence of observed Görtler vortices on the spray film is critically important for the processes of break-up, atomization, spray pattern formation, and spray uniformity. In figures 4.16 and 4.17, the mean and instantaneous spray film surface and velocity fields at the exit cross-section of all 3-D simulations. The Görtler vortices generate sequential negative and positive radial velocity fields. These fields create waves in the streamwise direction of the spray film. The amplitude and frequency of waves increase with rising Görtler number caused by increased Reynolds number. Furthermore, the mean free surfaces given in figures 4.16 and 4.17 settle in a time-independent specific location, and the film tears along the streamwise direction as the film gets thinner due to radial expansion of the spray film surface. These results clearly illustrate the strong relationship between the wavy film surface and the observed Görtler vortices, highlighting their significant role in the spray dynamics. Our simulations can not represent the atomization. However, the experimental study of Nural and Ertunç [20] clearly shows how streaks can cause non-uniform spray patterns.

Upon reevaluating the spray films used in the 2-D and 3-D simulations with a ring-like inlet, as shown in figure 4.1, it is evident that the averaged 3-D simulations produce thicker films than the 2-D simulations. This difference is attributed to the averaging effect of the wavy surface in the tangential direction.

Figure 4.16: *Instant and time-averaged VOF, free surface visualization of liquid interface with iso value =0.9 for the axial inlet.*

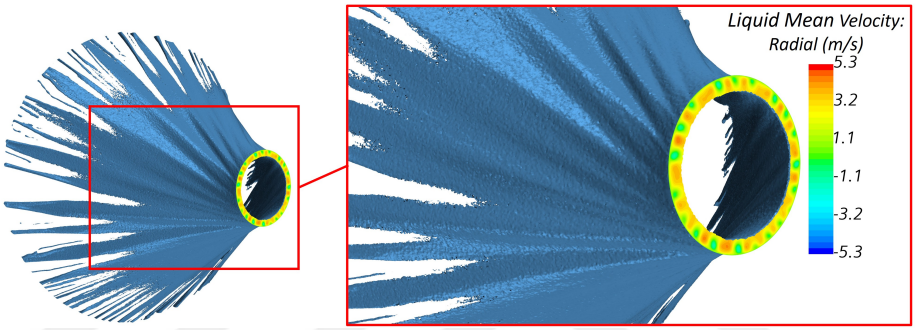

(a) Instantaneous at Re_{bulk} = 3582

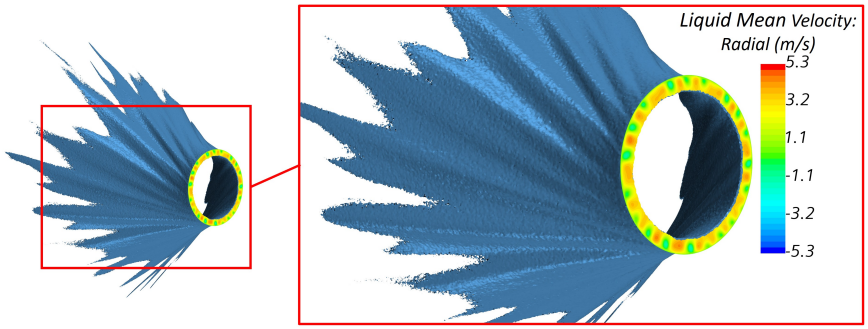

(b) Time averaged at Re_{bulk} = 3582

Figure 4.17: *Instant and time-averaged VOF, free surface visualization of liquid interface with iso value =0.9 of 3D ring-like inlet.*

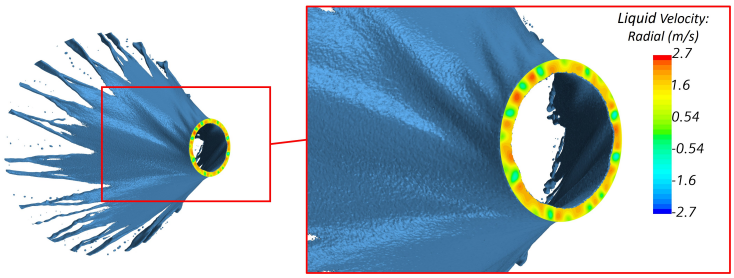

(a) Instantaneous at Re_{bulk} = 3582

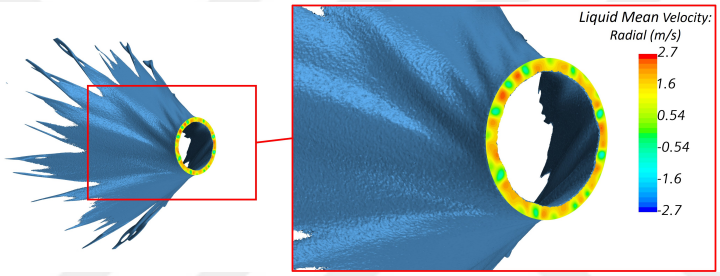

(b) Time averaged at Re_{bulk} = 3582

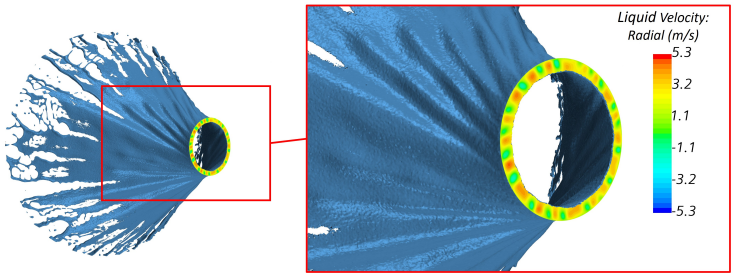

(c) Instantaneous at Re_{bulk} = 7163

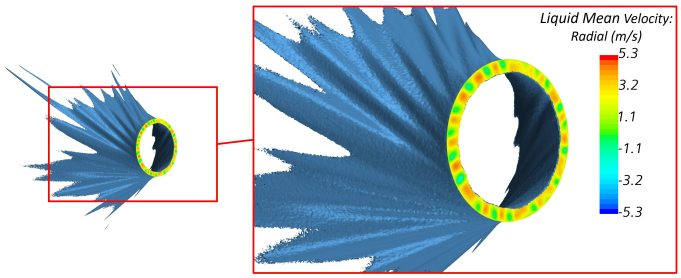

(d) Time averaged at Re_{bulk} = 7163

4.7 Blade Inlet PSA

The results of 3D ring-like simulation results of PSA indicate that the generation of uniform spray film may not be possible even if continuous inlet conditions are provided. Because Görtler vortices occur due to the exerted centrifugal force on swirling liquid film flow. However, the comparison of 2-D axisymmetric and 3D simulations shows that there are no significant differences in terms of PSA performance parameters (film thickness, spray angle, and pressure drop) and averaged liquid film velocity profiles when identical inlet conditions are supplied. Moreover, the studies of Bal and Maly report that the performance parameter results of close-type circular and rectangular port inlet PSA between experiments and 2D axisymmetric simulations converge when the same inlet flow conditions (angular momentum, kinetic energy, and mass flowrate) of the 3-D simulations are also provided in the 2-D axisymmetric simulations. However, the results of 2-D axisymmetric simulations could not capture the experimental results when the inlet conditions of the simulation are computed according to the conservation of mass, angular momentum, and kinetic energy with uniform inlet flow assumption. Uniform flow does not occur at the rectangular and circular port inlets due to the separation of flow inside the inlet and the narrowing flow due to the inertia of the flow in the swirl chamber. In the scope of these outcomes, an inlet geometry is designed to achieve flow conditions at the inlet, which have a uniform flow and are not affected by the inertia of the flow in the swirl chamber.

In the design of new inlet geometry, the advantages of helical and rectangular inlets are combined and avoided, as are their disadvantages. In rectangular inlets, the mass flow rate of the flow can be controlled by manipulating inlet depth while inlet flow direction and velocity are kept constant. However, separations in the inlet cannot be inhibited because of sharp corners at the inlet's entrance. Moreover, the angular momentum of the flow with respect to the center axis of PSA varies at the flow of the inlet because the angle

between the radial axis and the side walls of the rectangular inlet is different. Therefore, the flow enters the swirl chamber by narrowing because the swirling flow in the swirl chamber pushes the flow to the swirl chamber wall. These conditions result in a non-uniform flow at the inlet and disable non-uniform flow assumptions. It also generates 3-D flow structures in the flow, which causes spray uniformity. The same disadvantages are observed in the helical inlet. However, separating flow in the inlet is eliminated because of the curvy walls of the helical inlet. Flow is directed to the swirl chamber smoothly.

A blade inlet is designed to generate uniform flow at the inlet of open-end PSA shown in figure 4.18. The cross-section of geometry is rectangular so that the mass flow rate can be controlled by changing the depth of the inlet while inlet velocity and flow angle are kept constant. The flow is directed to the swirl chamber smoothly, like in a helical inlet. Uniform flow is provided in this way. The most important property of this inlet is that the angle of the side walls with the radial axis is the same $\theta_{w,1} = \theta_{w,2}$. With that configuration, the angular momentum of the flow with respect to the nozzle center axis at the entrance of the swirl chamber varies minimally from one side wall to the other side wall. Moreover, the contracting geometry of the blade inlet increases the inertia of the flow close to the inertia of the flow at the swirl chamber. With the provided high inertia and equal side wall angles, the narrowing problem of the flow at the swirl chamber entrance is minimized. Moreover, inlet flow angle θ_f can be assumed to be close to the side wall angle when the channel width of the inlet is narrow enough and the flow direction inlet condition of 2-D axisymmetric so that axisymmetric simulations can be carried out without performing 3-D simulations.

Figure 4.18: *Blade geometry of PSA.*

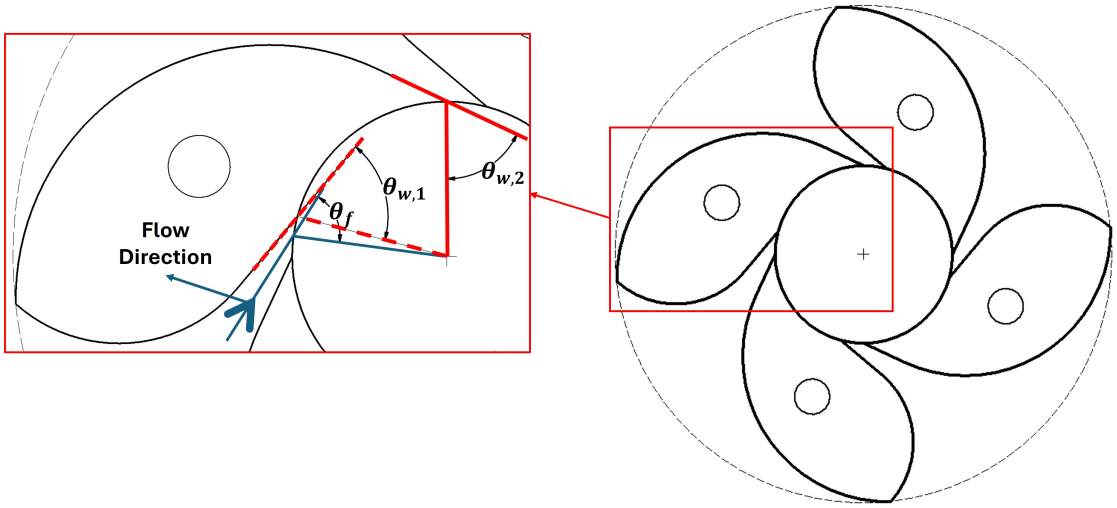

4.8 Performance Parameters of Blade Inlet PSA

The blade inlet simulation results indicate that blade type inlet can achieve uniform flow at the inlet shown in figure 4.19. The flow entrance angle is computed around $64.4°$ which shows the flow entrance angle converges to the wall angle, and its changes with varying mass flow rate are $0.2°$. If a flow angle is desired closer to the wall angle, it can be achieved by narrowing the channel width more. Moreover, the difference in entrance flow angle with respect to mass flowrate shows that once the entrance flow angle is determined for a single mass flow rate with 3D blade inlet simulations, there is no need to perform blade inlet simulations if viscous loss due to contracting flow in the blade inlet wants to be neglected. The viscous loss can be neglected for rough prediction in pressure drop because it is around $\%3$ of the experimental pressure drop result.

Figure 4.19: *Line Integral Convolution representation of 3-D blade inlet simulation at Re_{bulk} = 23358 cross-section perpendicular to PSA axial axis.*

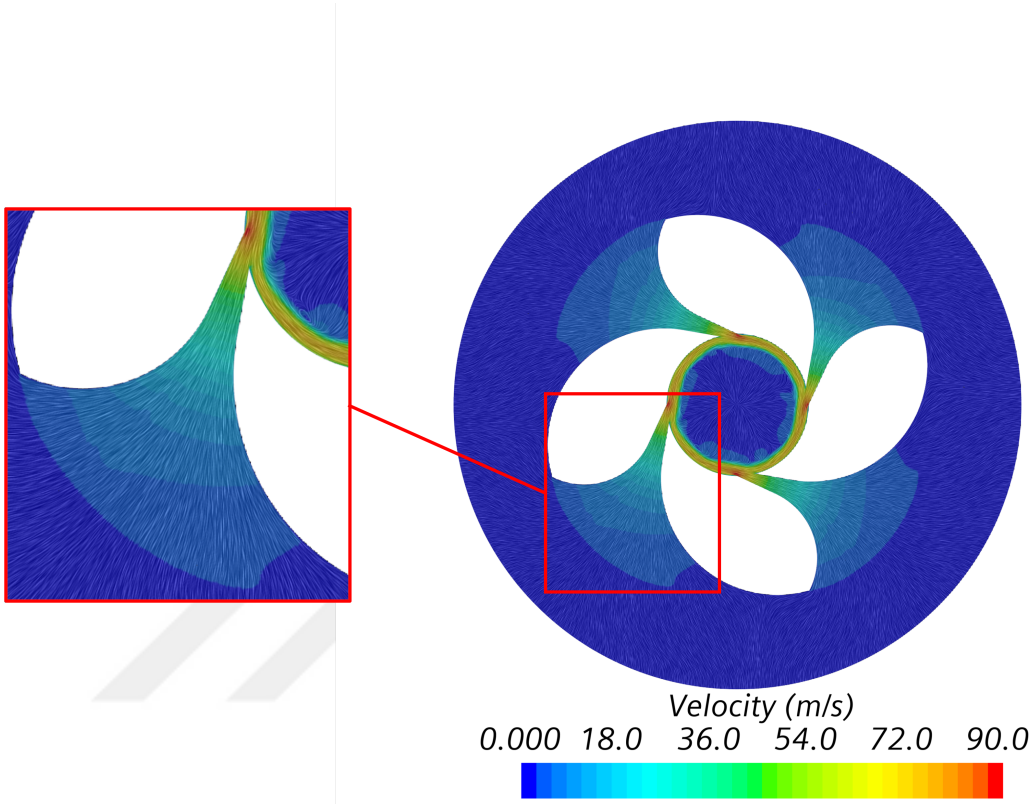

In pressure drop results shown in table 4.2, the error between the experimental results and simulations is around $\%8$. The pressure drop result of simulations is computed by adding The viscous loss and the dynamic pressure rise of the blade inlet were obtained in 3-D blade inlet simulations compared to the static pressure at the 2-D blade inlet obtained in 2-D blade inlet simulations. In experiments, gauge pressure measurements are performed before the flow enters the nozzle adaptor. Simulation results predicted a pressure drop lower than in the experiment. The error can arise from the 3-D vortex structures

in the swirling liquid film flow, which cannot be captured in 2-D axisymmetric simulation. First, in the study of Görtler vortex formation, it is seen that velocity profiles in 3-D simulation have linear velocity profiles near the exit of the orifice, which is different than velocity profiles of 2-D axisymmetric simulations due to the effect of Görtler vortices. In that study, the effect of the difference in velocity profile is not seen in the performance parameters of ring-like inlet PSA. Because the nozzle length of ring-like inlet PSA was $2mm$, and Görtler vortices are captured between $z = 1.365mm$ and $z = 2mm$ and its effect on velocity profile are obtained near the exit $z = 1.9mm$. It can be inferred that the effect of Görtler vortices on performance parameters is not obtained because its effect is revealed in a short distance. However, the nozzle length of blade inlet PSA is $10mm$, and the spray angle is around 64° which is rather higher than ring-like inlet PSA 33°. It can be understood that the ratio of tangential velocity to axial velocity is relatively higher in blade inlet PSA. As Schlichting reported, centrifugal force has a destabilizing effect. It can be inferred that Görtler vortices are likely to appear earlier in blade inlet PSA, and these vortex structures tend to persist for an extended distance. Therefore, viscous losses due to the Görtler vortices increase, which cannot be captured in 2-D axisymmetric simulations. These structures can depict different 3-D structures in the swirling liquid film flow of PSA. Finally, viscous loss in the blade inlet is computed with Quasi-DNS simulations. LES simulations can be required to capture the viscous loss of smaller eddies in the flow.

Table 4.2: *Comparison of pressure drop results between simulation and experimental data.*

Case	**Mass Flowrate [kg/s]**	Re_{bulk}	**Blade Viscous Loss [bar]**	**Nozzle Pressure Drop [bar]**	**Pressure Drop ΔP [bar]**	**Pressure Drop Error [%]**	**Pressure Drop Standard Deviation [bar]**
Simulation	0.1660	23358	0.91	30.77	31.68	7.73	—
Experiment	0.1660	23358	—	—	34.33	—	0.73
Simulation	0.1499	20875	0.78	25.19	25.97	7.21	—
Experiment	0.1499	20875	—	—	27.99	—	0.40
Simulation	0.1328	18512	0.66	19.60	20.26	8.15	—
Experiment	0.1328	18512	—	—	22.06	—	0.2
Simulation	0.1179	16389	0.54	15.43	15.97	8.31	—
Experiment	0.1179	16389	—	—	17.42	—	0.08
Simulation	0.0997	13683	0.42	10.96	11.38	8.30	—
Experiment	0.0997	13683	—	—	12.41	—	0.11

A non-physical local zone is determined in the absolute pressure field. The absolute pressure drops to negative after near the inlet due to separating flow when Re_{bulk} is above 16389, as shown in figure 4.20. The reason for the negative absolute pressure can be originated from cavitation in the flow. Moreover, popping noises are obtained during the experiment when Re_{bulk} is above 18512. However, the error between simulations and experiments in performance parameters does not change with negative absolute pressure.

Figure 4.20: *Absolute pressure fields of 2-D blade inlet PSA simulations.*

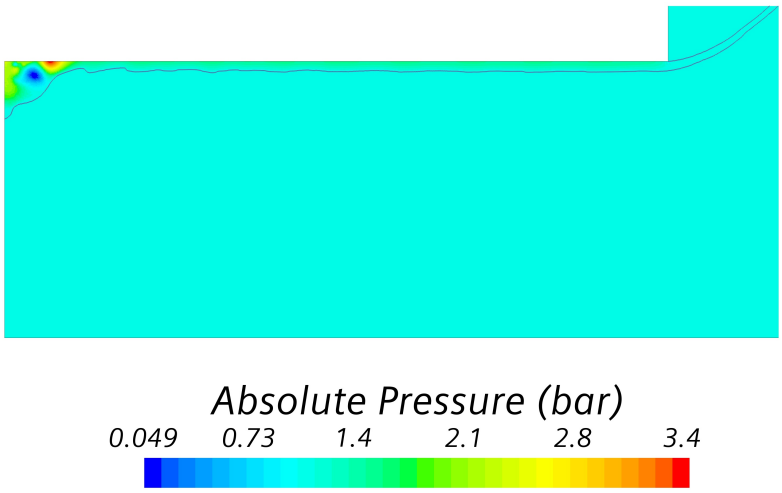

(a) Re_{bulk} = 13683

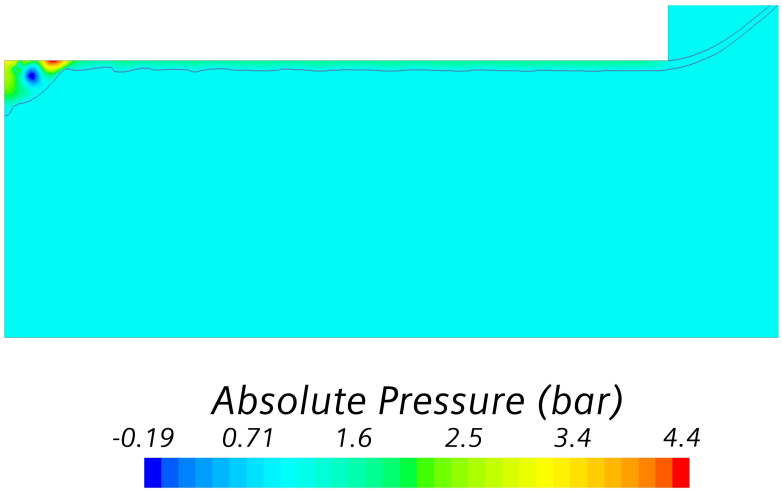

(b) Re_{bulk} = 16389

In a comparison of spray angle shown in table 4.3 between the simulations and experiments, a 6° error is determined, which is $\%10$ of experimental results. When the spray film is observed, it is obtained that the spray film in experiments is more unstable than in the simulations shown in figure 4.21. In the formation of spray film, swirling liquid film inside the nozzle is ejected from the orifice with tangential and axial velocity components. After this ejection, the tangential velocity component of the fluid film rapidly converted into radial velocity. During the conversion, a hollow cone-shaped spray film occurs. However, hollow cone spray film continues to rotate and get thinner due to the conservation of angular momentum and mass until it breaks up. After the breakup, the tangential velocity of the liquid is totally converted into radial velocity. The observed unstable behavior on the spray film in experiments can cause early tears in the spray film. Therefore, its radial velocity is converted into tangential velocity earlier than the simulations, and the spray angle is captured higher. The liquid film inside the nozzle is computed around $220\mu m$, which is quite thin with respect to the nozzle diameter, and the spray angle is relatively high. In these conditions, capturing more accurate spray angle results is challenging for staff because minor disturbances can grow faster due to the thin film, and high spray angle results in immediate thinning of spray film due to the cone shape of spray film and conservation of mass. Tears of spray film can occur due to the properties explained above. It is expected that spray angle can be predicted more accurately in lower spray angles and relatively thick liquid film.

Table 4.3: *Comparison of half spray angle results between simulation and experimental data.*

Case	**Mass Flowrate [kg/s]**	$Re_{\textbf{bulk}}$	**Inlet Flow Angle θ_f[°]**	**Half Spray Angle [°]**	**Half Spray Angle Error [°]**
Simulation	0.1660	23358	64.41	57.98	5.66
Experiment	0.1660	23358	—	63.64	—
Simulation	0.1499	20875 0.0721	64.40	58.30	6.26
Experiment	0.1499	20875	—	64.56	—
Simulation	0.1328	18512	64.34	57.83	6.33
Experiment	0.1328	18512	—	64.16	—
Simulation	0.1179	16389	64.33	58.00	5.79
Experiment	0.1179	16389	—	63.79	—
Simulation	0.0997	13683	64.25	58.46	6.40
Experiment	0.0997	13683	—	64.86	—

Figure 4.21: *Spray film comparison between experiment and simulation where* Re_{bulk} = *23358.*

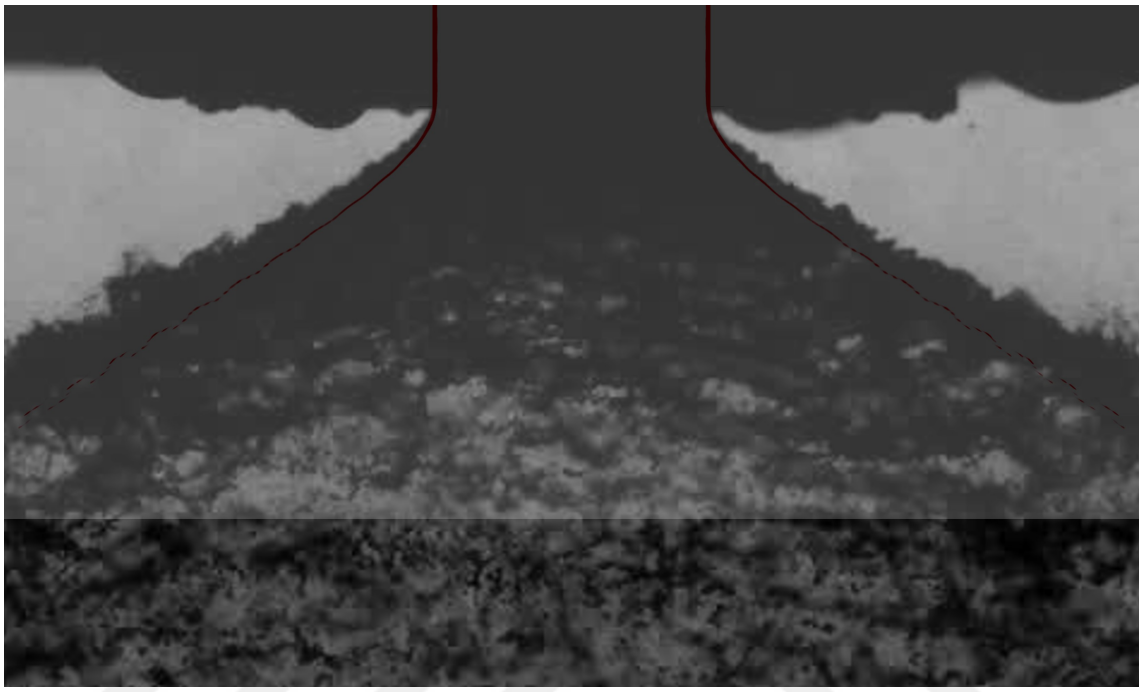

5. CONCLUSIONS

This study investigates the flow and spray uniformity of open-end PSA in ideal inlet conditions. For the analysis, high-fidelity 3-D CFD simulations were performed. Ideal inlet conditions are provided using an axisymmetric ring-like surface inlet to eliminate primary structures arising from the jet-jet interaction of finite-number port inlets. Nural indicates that these jet interactions severely affect spray uniformity. In the results of 3-D simulations obtained, Görtler vortices form in the swirling liquid film flow, and they cause wrinkled waves in the spray film. The analysis of Görtler vortex formation observed that separation near the inlet initiates these vortices. An additional axial swirling film flow inlet simulations are performed to investigate the formation of Görtler vortices without separating flow.

Bal and Maly report that non-uniform flow at the inlet ports of PSA disables prediction of PSA performance parameters by conducting 2-D axisymmetric simulations because of non-identical inlet conditions. Moreover, 3-D Görtler vortices obtained in the 3-D simulations raise concerns about the validity of 2-D axisymmetric simulations in predicting PSA performance parameters. 2-D axisymmetric simulations are carried out, and its results are compared with the 3-D ring-like inlet PSA simulations. The comparison is performed on average velocity distribution, pressure drop, film thickness, and spray film.

2-D and 3-D comparison of results motivates us to design an inlet geometry that provides similar inlet conditions with a ring-like inlet. The blade-type inlet is designed for this objective. 3-D blade simulations are conducted to analyze the characteristics and flow properties of the blade inlet. The validity performance of 2-D axisymmetric simulations is analyzed when blade-type inlets are used in open-end PSA by conducting spray angle and pressure drop results of simulations with experimental study.

The findings obtained in this study are summarized below,

Formation of Görtler Vortices and Its Impact on the Flow in Comparison to Two-Dimensional Axisymmetric Simulations

- Görtler vortices can form in open-end PSAs at Görtler numbers that are close to what Liepmann has suggested.
- 2-D and 3-D simulations with identical ring-like inlets show almost identical primary performance parameters such as pressure drop, spray angle, and film thickness. The slight differences in the velocity profiles are due to the Görtler vortices, which the 2-D simulations can not capture.
- Görtler vortices induce waves on the issued spray film, which might cause a streaky breakup and non-uniform sprays.
- Extremely low-pressure drop of an axial-swirling inlet compared to a ring-like inlet.

Blade Type Inlet Open-End Pressure Swirl Atomizer

- Uniform flow at the inlet can be achieved with blade inlets
- Pressure drop of blade inlet PSA can be predicted with 8% deviation while the half spray angle is predicted with 6°.
- Görtler vortex can be the source of pressure drop error in 2- D blade inlet PSA simulations. Decay in averaged velocity profiles of 3-D ring-like inlet simulations near the orifice, which is indicated in comparison to 2-D and 3-D ring-like inlet simulations. With the increasing nozzle length of blade inlet PSA compared to ring-like inlet PSA, decay in velocity profiles can be raised.
- Non-captured instabilities, which are seen in the surface of spray film in 2-D simulations of the spray film, can lead to inaccuracies in the half spray angle.

- Non-physical negative absolute pressure is observed locally in 2-D simulations. The negative absolute pressure field can point to cavitation in that field. Popping noises, which can occur due to cavitation, are also observed during the experiment.

In future work, parametric studies will be performed to characterize blade inlet PSA. Additionally, separation near the inlet will be removed by implementing a new geometric design. The visualization of Görtler vortices in the open-end PSA could not be performed directly but rather inferred through secondary effects, such as their influence on the heat transfer coefficient or spray film geometry. Finally, shear stresses on the wall induced by Görtler vortices will be parametrized.

REFERENCES

[1] M. Suyari and A. Lefebvre, "Film thickness measurements in a simplex swirl atomizer," *Journal of Propulsion and Power*, vol. 2, no. 6, pp. 528–533, 1986.

[2] Q. fei Fu, L. jun Yang, and X. dong Wang, "Theoretical and experimental study of the dynamics of a liquid swirl injector," *Journal of Propulsion and Power*, vol. 26, pp. 94–101, January–February 2010.

[3] A. Yule and J.J.Chinn, "The internal flow and exit conditions of pressure swirl atomizer," *Atomization and Sprays*, vol. 10, pp. 121–146, 2000.

[4] W. Qian, X. Hui, C. Zhang, Q. Xu, and Y. Lin, "A numerical study of the internal flow in a pressure swirl atomizer," *Turbomachinery Technical Conference and Exposition*, June 2017.

[5] Q. fei Fu, L. jun Yang, and Y. yuan Qu, "Measurement of annular liquid film thickness in an open-end swirl injector," *Aerospace Science and Technology*, vol. 15, pp. 117–124, March 2011.

[6] Q.-F. Fu, L.-J. Yang, W. Zhang, and K.-D. Cui, "Spray characteristics of an open-end swirl injector," *Atomization and Sprays*, p. 431–445, 2012.

[7] C. W. Hirt and B. D. Nichols, "Volume of fluid (vof) method for the dynamics of free boundaries," *Journal of Computational Physics*, vol. 39, pp. 201–225, 1981.

[8] O. Mahrenholtz and M. Markiewicz, *Nonlinear Water Wave Interaction*. WIT Press, 1999.

[9] M. Sussman, E. Fatemi, P. Smereka, and S. Osher, "An improved level set method for incompressible two-phase flows," *Computers and Fluids*, vol. 27, p. 663–680, 1998.

[10] M. Sussman and E. G. Puckett, "A coupled level set and volume-of-fluid method for computing 3d and axisymmetric incompressible two-phase flows," *Journal of Computational Physics*, p. 301–337, 2000.

[11] A. Ashraf, I. Milind, and A. Jog, "Nonlinear breakup model for a liquid sheet emanating from a pressure-swirl atomizer," *Journal of Engineering for Gas Turbines and Power*, vol. 129, p. 945–953, 2007.

[12] M. Bal, G. Kayansalçik, Özgür Ertunç, and Y. E. Böke, "Benchmark study of 2d and 3d vof simulations of a simplex nozzle using a hybrid rans-les approach," *Fuel*, vol. 319, 2022.

[13] M. Maly, J. Slama, O. Cejpek, and J. Jedelsky, "Searching for a numerical model for prediction of pressure-swirl atomizer internal flow," *Applied Sciences*, vol. 12, 2022.

[14] O. E. Nural, *Developing a methodology for the design and optimization of the pressure-swirl atomizers*. PhD thesis, Ozyegin University, 2023.

[15] H. Schlichting, *Boundary-Layer Theory*. McGraW-Hill, 1970.

[16] H. Görtler, "On the three-dimensional instability of laminar boundary layers on concave walls," *NACA*, 1940.

[17] H. W. Liepmann, "Investigation of boundary layer transition on concave walls," *NACA*, 1945.

[18] A. Razeghi and Ö. Ertunç, "Numerical investigation of multiphase flow inside a pressure swirl atomizer at the initial stage of injection," *Atomization and Sprays*, vol. 28, pp. 417–441, 2018.

[19] H. A. Vaidya, Ö. Ertunç, B. Genç, F. Beyer, Ç. Köksoy, and A. Delgado, "Numerical simulations of swirling pipe flows- decay of swirl and occurrence of vortex structures," *13th European Turbulence Conference (ETC13)*, 2011.

[20] O. E. Nural and Ö. Ertunç, "Circumferential spray patternation of the pressure swirl atomizers," *Research Square*, 2023.